

Modeling the angular correlation function and its full covariance in Photometric Galaxy Surveys

Martín Crocce¹, Anna Cabré² & Enrique Gaztañaga¹

¹ *Institut de Ciències de l'Espai, IEEC-CSIC, Campus UAB, Facultat de Ciències, Torre C5 par-2, Barcelona 08193, Spain*

² *Center for Particle Cosmology, University of Pennsylvania, 209, South 33rd Street, Philadelphia, PA, 19104, USA*

22 October 2018

ABSTRACT

Near future cosmology will see the advent of wide area photometric galaxy surveys, like the Dark Energy Survey (DES), that extent to high redshifts ($z \sim 1 - 2$) but with poor radial distance resolution. In such cases splitting the data into redshift bins and using the angular correlation function $w(\theta)$, or the C_ℓ power spectrum, will become the standard approach to extract cosmological information or to study the nature of dark energy through the Baryon Acoustic Oscillations (BAO) probe. In this work we present a detailed model for $w(\theta)$ at large scales as a function of redshift and bin width, including all relevant effects, namely nonlinear gravitational clustering, bias, redshift space distortions and photo- z uncertainties. We also present a model for the full covariance matrix characterizing the angular correlation measurements, that takes into account the same effects as for $w(\theta)$ and also the possibility of a shot-noise component and partial sky coverage. Provided with a large volume N-body simulation from the MICE collaboration we built several ensembles of mock redshift bins with a sky coverage and depth typical of forthcoming photometric surveys. The model for the angular correlation and the one for the covariance matrix agree remarkably well with the mock measurements in all configurations. The prospects for a full shape analysis of $w(\theta)$ at BAO scales in forthcoming photometric surveys such as DES are thus very encouraging.

1 INTRODUCTION

The statistical analysis of the distribution of structure at large astronomical scales has played a key role in advancing the field of Cosmology over the last 20 years. From shaping our understanding of complex processes driving galaxy formation and evolution to constraining the energy density content of the Universe.

The completion of large extra-galactic surveys such as the Sloan Digital Sky Survey (SDSS, York et al. 2000) and the 2dF Galaxy Redshift Survey (2dFGRS, Colless et al. 2003) have bolstered our general knowledge in the field. Particularly more so when combined with the precise measurements of the Cosmic Microwave Background or the increasingly reach data from Supernova data (Sánchez et al. 2009; Percival et al. 2010; Reid et al. 2010; Komatsu et al. 2010). One of the most promising, and eventually rewarding, challenges for the field of large scale structure today is the prospect for determining what drives the late time acceleration of the Universe (Riess et al. 1998; Perlmutter et al. 1999). This is probed by the presence, in the clustering pattern of galaxies, of remanent features from the coupling of baryon and photons prior to recombination known

as the Baryon Acoustic Oscillations (BAO). The BAO have already been detected in the spectroscopic samples of Luminous Red Galaxies (LRGs) in both SDSS and 2dFGRS (Cole et al. 2005; Eisenstein et al. 2005), and studied in the early imaging data of SDSS (Padmanabhan et al. 2007).

But the observational quest has only started. Several of the next-generation surveys will gain in area and depth, in exchange for a poorer determination of radial positions. In turn this imposes the need for angular clustering analysis in redshift bins of width few times larger than that of the photometric error uncertainty at the given redshifts. The difficulty lies in that the projection in redshift bins lowers the clustering amplitude, erasing any particular feature and increasing the noise-to-signal ratio. The achievable precision of our photometrically estimated redshift will play a crucial role. We thus need to understand what affects the angular clustering pattern more severely.

The aim of our work is to tackle this problem, providing a well calibrated model for the clustering signal at large-scales as a function of angle, radial distance and bin width, deepening the available literature in the subject (e.g. Padmanabhan et al. 2007, Blake et al. 2007 and references

therein). We put particular effort in stressing the most relevant effects, redshift distortions and photo-z uncertainties, and how they interplay.

An equally important problem is to have the capability of estimating the full errors of the measurements. We thus provide a well tested description of the complex error matrix characterizing the measurements of the correlation function in real situations, i.e. including effects of partial sky coverage, photo-z, redshift distortions, bias and shot-noise.

Both, the model for the correlation and the one for the error matrix, will be extensively tested against a very rich set of mocks redshift bins. This work should therefore be relevant for ongoing projects that use photometric redshift estimates like the Dark Energy Survey¹ (DES), the Physics of the Accelerating Universe collaboration² (PAU) and the the Panoramic Survey Telescope and Rapid Response System³ (PanStarrs). But also for upcoming imaging proposals such as the Large Synoptic Survey Telescope⁴ (LSST) and the ESA/Euclid⁵ survey.

This paper is organized as follows. In Sec. 2 and Sec. 3 we discuss the models proposed in this work for the angular correlation function and its full error matrix respectively. In Sec. 4 we describe the set of ensembles of mock redshift bins implemented using a large volume N-body simulation. In Sec. 5 and 6 we test the models against the mocks, under different regimes and assumptions. Section 7 contains our conclusions and future lines of research. We also include several appendixes. In Appendix A we give a description of our model for the 3-d nonlinear matter correlation function. In Appendix B we study the limitations of the widely used Limber approximation. Finally, Appendix C gives a brief note on the covariance of the angular power spectrum induced by partial sky coverage.

2 AN ANALYTIC MODEL FOR THE ANGULAR CORRELATION FUNCTION

Let us start by considering the projection of the spatial galaxy fluctuations $\delta_g(\mathbf{x}, z)$ along a given direction in the sky $\hat{\mathbf{n}}$

$$\delta(\hat{\mathbf{n}}) = \int dz \phi(z) \delta_g(\hat{\mathbf{n}}, z), \quad (1)$$

where ϕ is the radial selection function. The angular correlation function is then obtained as a simple projection of the 3-d correlation function ξ (Peebles 1973),

$$\begin{aligned} w(\theta) &\equiv \langle \delta_g(\hat{\mathbf{n}}) \delta_g(\hat{\mathbf{n}} + \hat{\theta}) \rangle = \\ &= \int dz_1 \phi(z_1) \int dz_2 \phi(z_2) \xi_{gg}(r(z_1), r(z_2), \theta) \end{aligned} \quad (2)$$

where θ is the angle between directions $\hat{\mathbf{n}}$ and $\hat{\mathbf{n}} + \hat{\theta}$, related to the pair-separation through

$$r_{12}(\theta) = \{r(z_1)^2 + r(z_2)^2 - 2r(z_1)r(z_2)\cos(\theta)\}^{1/2} \quad (3)$$

and $r(z)$ is the co-moving distance to redshift z given by

$$r(z) = \int_0^z \frac{c}{H(u)} du, \quad (4)$$

where $H(z)/H_0 = \sqrt{\Omega_m(1+z)^3 + \Omega_{DE}(1+z)^{3(1+w)}}$ is the Hubble parameter, Ω_m and $\Omega_{DE} = 1 - \Omega_m$ are the matter and dark energy densities respectively, and w is the dark energy equation of state⁶. Since we are interested in redshift bins and not in extended selections we can neglect the growth evolution within the bin and simply evaluate the 3-d correlation in some fiducial redshift \bar{z} (e.g. the mean redshift of the bin, weighted by ϕ). In addition we will assume a *local and linear bias* relation between fluctuations in the tracer (e.g. galaxies) and matter density field, $\delta_g = b(z)\delta$ (see Sec. 5.2 for a justification). Under these assumptions Eq. (2) is converted to

$$w(\theta) = \int dz_1 f(z_1) \int dz_2 f(z_2) \xi(r(z_1), r(z_2), \theta, \bar{z}) \quad (5)$$

where $f(z) \equiv b(z)\phi(z)$ and ξ is the matter 3-d correlation function.

Hence, in order to predict $w(\theta)$ we need a model for the spatial clustering accurate in a sufficiently large range of scales to allow the projection in Eq. (5), in particular when photo-z errors broadens the extent of the radial distribution (see (Sánchez et al. 2010) for a empirical parametric fit suited for BAO scales).

In what follows we discuss how to include photo-z effects and the model for spatial clustering in real and redshift space that we will use throughout this paper.

2.1 Photo-z

We incorporate the way uncertainties in the true redshift positions obtained from photometric estimates affect angular clustering by means of the radial selection function, following Budavari et al. 2003 (see also Ma et al. 2006).

The radial selection ϕ is the probability to include a galaxy in our redshift bin. If the selection of objects is done according to their true redshifts, then ϕ is equal to the true number of galaxies per unit redshift times a window function W encoding selection characteristics (e.g. redshift cuts),

$$\phi(z) = \frac{dN_g}{dz} W(z). \quad (6)$$

Instead, if the selection is done according to photometric redshift estimates, one must incorporate the probability $P(z|z_p)$ for the true redshift to be z when the photometric one is z_p . The ending result is the product (Budavari et al. 2003),

$$\phi(z) = \frac{dN_g}{dz} \int dz_p P(z|z_p) W(z_p), \quad (7)$$

¹ www.darkenergysurvey.org

² www.pausurvey.org

³ pan-stars.ifa.hawaii.edu

⁴ www.lsst.org

⁵ www.euclid-imaging.net

⁶ These expressions explicitly assume a flat cosmology and constant w , for more general cases see (Matsubara 2004) and references therein

where $W(z_p)$ is the photometric redshift window function. Throughout this paper we will only consider top-hat window functions both in true and photometric redshifts (i.e. $W = 1$ within a given redshift range, and 0 otherwise). In addition we will only consider the idealized case where the photometric estimate is Gaussianly distributed around the true redshift (e.g. Ma et al. 2006). Although this might be far from reality, it serves as an interesting starting point for more realistic scenarios (Hearin et al. 2010; Bernstein & Huterer 2010). Lastly, we recall that ϕ should be normalized to unity within the redshift range of interest.

2.2 Spatial clustering and redshift evolution

We now turn into the discussion of the 3-d matter correlation model accounting for *nonlinear gravitational effects, redshift space distortions*, and the way we evolve it with redshift. We postpone to Appendix A the testing of this model against measurements of 3-d matter clustering in N-body simulations.

The linear evolution of the clustering pattern preserves its shape but increases the overall amplitude. The main effects due to nonlinear gravitational clustering at large scales are a smoothing of the BAO wiggles and a rise in clustering amplitude above linear values towards smaller scales due to mode-coupling effects (Seo & Eisenstein 2005; Eisenstein et al. 2007; Crocce and Scoccimarro 2008). Although these processes can be modeled from first principles (Crocce and Scoccimarro 2006a; Matarrese & Pietroni 2008; Matsubara 2008; Taruya et al. 2009), it is also possible and desirable to find simpler parametric approximations. In the correlation function these two effects can be parameterized as (Crocce and Scoccimarro 2008),

$$\xi(r) = [\xi_{\text{Lin}}(r) \otimes e^{-(r/s_{\text{bao}})^2}](r) + A_{\text{mc}} \xi_{\text{Lin}}^{(1)}(r) \xi'_{\text{Lin}}(r) \quad (8)$$

where s_{bao} and A_{mc} are fitting parameters, ξ_{Lin} is the linear correlation function at the given redshift, ξ'_{Lin} its derivative and

$$\xi_{\text{Lin}}^{(1)} \equiv 4\pi \int P_{\text{Lin}}(k, z) j_1(kr) k dk. \quad (9)$$

In Eq. (8), the symbol \otimes denotes a convolution. This model have been already used in the analysis of matter, halo and galaxy clustering (Sánchez et al. 2008; Sánchez et al. 2009).

However the standard approach for analyzing clustering data in a photometric redshift survey covering from low ($z \sim 0.2$) to high redshift ($z \sim 1.4$) is to divide the data into several redshift bins (whose minimum width are ultimately determined by the photo- z accuracy, e.g. Padmanabhan et al. 2007). If one then performs a joint analysis of all these bins it is desirable to have the least number of nuisance parameters possible in order to optimize constraints on derived cosmological parameters. From this point of view it is interesting to investigate to what extent a single set of best-fit parameters can be used to describe the 3-d clustering from low to high redshift, and hence the angular clustering after the projection in Eq. (5).

We implement this as follows. The first term in Eq. (8) is proportional to the linear correlation, therefore it scales with

the growth factor squared $\sim D^2(z)$. The second term arises from leading order mode-mode coupling and thus scales as $\sim D^4(z)$. In turn the damping of BAO is proportional to the amplitude of large-scale velocity flows, Eq. (A1), and so $s_{\text{bao}} \sim D(z)$. Putting these considerations together we scale our parametric model with redshift as,

$$\begin{aligned} \xi(r, z) &= D^2(z) [\xi_{\text{Lin},0}(r) \otimes e^{-(r/D(z)s_{\text{bao}})^2}](r) \\ &+ A_{\text{mc}} D^4(z) \xi_{\text{Lin},0}^{(1)}(r) \xi'_{\text{Lin},0}(r) \end{aligned} \quad (10)$$

where sub-script 0 means (linear) quantities evaluated at $z = 0$. The values for s_{bao} and A_{mc} can be taken from a best-fit analysis to $\xi(r)$ at any given redshift (or to $w(\theta)$ in any given redshift bin, after the projection in Eq. (5)). In our case will be those from the best-fit at $z = 0.3$, $s_{\text{bao}} = 6.37 h^{-1} \text{Mpc}$ and $A_{\text{mc}} = 1.55$. This is detailed in Appendix A, where we present a detailed comparison of our model against numerical simulations, with particular emphasis on the scaling introduced in Eq. (10).

Lastly, we move to the inclusion of redshift space distortions. The true distance to a galaxy differs from the one derived from its redshift through the Hubble law because of the radial peculiar velocity of the galaxy on top of the Hubble flow (Kaiser 1987). At large scales, the coherent infall of galaxies into large overdensities, such as clusters, make their observed radial separation smaller, squashing the structure along the line-of-sight and boosting the amplitude of the 3-d two point correlation. In this way for separations along the line of sight $\pi \lesssim 40 h^{-1} \text{Mpc}$ the correlation (or number of pairs) increases dramatically, while for larger separations the correlation becomes negative in such a way that the total number of pairs along the l.o.s is preserved (e.g. Fig. A1 in Gaztañaga et al. 2009). This implies that, by dividing the data in redshift bins, one is discarding the leverage of large radial separations effectively increasing the (angular) correlation within the bin (see Nock et al. 2010 for a recent and detailed discussion of this effect).

The linear redshift distortions discussed above, namely the Kaiser effect, can be easily described assuming the plane-parallel approximation. We will incorporate it into our modeling of the angular correlation function by writing $\xi(r_1, r_2) = \xi(\sigma, \pi)$ in Eq. (2), with (Hamilton 1992),

$$\xi(\sigma, \pi) = \xi_0(s)P_0(\mu) + \xi_2(s)P_2(\mu) + \xi_4(s)P_4(\mu), \quad (11)$$

where $\pi = r_2 - r_1$ and $\sigma^2 = 2r_1r_2(1 - \cos\theta)$ (to yield $s = r_{12}$) are the pair-separation along and transverse to the line-of-sight, $\mu = \pi/s$ and P_ℓ are the Legendre polynomials. The double integrals in Eq. (2) are still performed in the r_1, r_2 , variables leaving the evaluation of the radial selection functions unchanged. The monopoles of the anisotropic correlation $\xi_i(s)$ are given in Appendix B2 (Eqs. B10,B11,B12) in terms of the 3-d monopole correlation $\xi(s)$, that we will take as the one including nonlinear gravitational effects given by Eq. (10). In Appendix B2 we discuss this effect in more detail, also in the context of the Limber approximation.

3 ANALYTICAL MODELING OF THE COVARIANCE MATRIX OF $W(\theta)$

An equally important aspect to the understanding of the signal in clustering analysis of galaxy surveys is the capability to estimate the corresponding errors in the measurements. This is of particular importance for analysis that use correlation functions in Configuration space because the measurements are highly correlated.

Notably there is scarce work in the literature aiming at developing analytical estimates of the covariance matrix of angular correlation functions besides the early work of Bernstein 1994, who developed an error estimate for the Landy & Szalay estimator in terms of higher order correlations.

Most “data analysis” papers have relied on subsampling techniques of the data itself, such as jack-knife, bootstrap and field-to-field variations (e.g. Ross et al. 2007; Meneux et al. 2009; Sawangwit et al. 2009). However as noted in the comprehensive work of Norberg et al. 2009 all these approaches have failings, at least in 3-d clustering, depending on the way they are implemented and the regime of scales of interest. On the other hand, projection along the line-of-sight alleviates this tension leading to a good agreement with theoretical estimates, as shown by Cabré et al. 2007 in the context of cross-correlations between galaxy and CMB maps.

In what follows we try to revert the lack of analytical work provided that we are interested on large angular scales, where nonlinear (i.e. non-Gaussian) effects are weaker and that we know how to model the signal itself. We thus concentrate in discussing how to model expected errors in angular clustering, including the effects of sampling variance, shot-noise, partial sky coverage, photo-z and redshift distortions. We put particular emphasis on the description of the full error matrix, and not only the diagonal components, and leave for further work the assessment of possible systematic effects.

Let us start by decomposing the fluctuations in the number of objects “per pixel” in the sky into spherical coordinates (Peebles 1973),

$$\delta(\hat{\mathbf{n}}) = \sum_{\ell \geq 0} \sum_{m=-\ell}^{\ell} a_{\ell m} Y_{\ell m}(\hat{\mathbf{n}}), \quad (12)$$

where $\hat{\mathbf{n}}$ is the line-of-sight direction and $Y_{\ell m}$ the spherical harmonics. The coefficients in this expansion form the *angular power spectrum*,

$$\langle a_{\ell m} a_{\ell' m'} \rangle \equiv \delta_{\ell \ell'} \delta_{m m'} C_{\ell} \quad (13)$$

that can be related to the *angular correlation function* using the Addition theorem⁷ yielding,

$$w(\theta) = \sum_{\ell \geq 0} \left(\frac{2\ell+1}{4\pi} \right) P_{\ell}(\cos\theta) C_{\ell} \quad (14)$$

where P_{ℓ} are the Legendre polynomials of degree ℓ . The covariance in the measurements of $w(\theta)$ can then be related

⁷ $P_{\ell}(\hat{\mathbf{n}} \cdot \hat{\mathbf{n}}') = \frac{4\pi}{2\ell+1} \sum_{m=-\ell}^{\ell} Y_{\ell m}(\hat{\mathbf{n}}) Y_{\ell m}^*(\hat{\mathbf{n}}')$

to those in C_{ℓ} as,

$$\text{Cov}_{\theta\theta'} = \sum_{\ell, \ell' \geq 0} \left(\frac{2\ell+1}{4\pi} \right)^2 P_{\ell}(\cos\theta) P_{\ell'}(\cos\theta') \text{Cov}_{\ell\ell'} \quad (15)$$

where

$$\text{Cov}_{\theta\theta'} \equiv \langle \tilde{w}(\theta) \tilde{w}(\theta') \rangle, \quad \text{Cov}_{\ell\ell'} \equiv \langle \tilde{C}_{\ell} \tilde{C}_{\ell'} \rangle, \quad (16)$$

and $\tilde{w}(\theta)$ and \tilde{C}_{ℓ} denote the estimators used for $w(\theta)$ and C_{ℓ} respectively. In a full sky situation, and assuming the $a_{\ell m}$ spectra are Gaussianly distributed, the \tilde{C}_{ℓ} measurements are uncorrelated, $\text{Cov}_{\ell\ell'} = \text{Var}(C_{\ell}) \delta_{\ell\ell'}$. In addition, one can estimate each ℓ power using the $2\ell+1$ available modes,

$$\tilde{C}_{\ell} \equiv \frac{1}{2\ell+1} \sum_{m=-\ell}^{\ell} a_{\ell m}^2 \quad (17)$$

thus, $\text{Var}(C_{\ell}) = 2C_{\ell}^2/(2\ell+1)$. Replacing these relations back into Eq. (15) leads to the final expression for $\text{Cov}_{\theta\theta'}$ in a full sky survey.

However a more realistic and interesting scenario is one in which the sky coverage is partial. In Cabré et al. 2007 it was shown, using Gaussian realizations of the $a_{\ell m}$ spectra, that errors in configurations space scale as $1/\sqrt{f_{\text{sky}}}$ (which, in turn, is the scaling of the available number of harmonic modes). In what follows we will assume this scaling, and compute the covariance matrix as (Dodelson 2003; Cabré et al. 2007)

$$\text{Cov}_{\theta\theta'} = \frac{2}{f_{\text{sky}}} \sum_{\ell \geq 0} \frac{2\ell+1}{(4\pi)^2} P_{\ell}(\cos\theta) P_{\ell}(\cos\theta') (C_{\ell} + 1/\bar{n})^2 \quad (18)$$

where we have also included the standard shot-noise contribution arising in the variance of the C_{ℓ} estimates (Peebles 1973) (\bar{n} is the number of objects per steradian). We remark that the assumption leading to Eq. (18) is *not* that the C_{ℓ} covariance remains diagonal in a partial sky survey but instead that $\text{Cov}(\theta, \theta')$ can be obtained from its full sky expression by the scaling $1/f_{\text{sky}}$. We discuss this further in Appendix C.

To proceed further we thus need a model for the angular spectra. In *real space* the C_{ℓ} spectra are given by (see Appendix A)

$$C_{\ell, \text{Exact}} = \frac{1}{2\pi^2} \int 4\pi k^2 dk P(k) \Psi_{\ell}^2(k) \quad (19)$$

where $P(k)$ is the real space matter power spectrum and,

$$\Psi_{\ell}(k) = \int dz \phi(z) D(z) j_{\ell}(kr(z)). \quad (20)$$

Throughout this paper we will use the *linear* theory power spectrum in Eq. (19). We have tested that the inclusion of small scale nonlinear effects (or the damping of the baryon acoustic features) have no impact in our predictions for the errors at the (large) angular scales we are interested in.

Redshift space distortions are accounted for by following the same procedure that leads to the C_{ℓ} expression in Eq. (19) but starting from a power spectrum that includes the Kaiser effect discussed in Sec. 2.2 and Eq. B8. The final result is simply the following additive contribution to the

kernel in Eq. (20) (Padmanabhan et al. 2007),

$$\Psi_\ell^r(k) = \beta \int dz \phi(z) D(z) \left[\frac{(2\ell^2 + 2\ell - 1)}{(2\ell + 3)(2\ell - 1)} j_\ell(kr) - \frac{\ell(\ell - 1)}{(2\ell - 1)(2\ell + 1)} j_{\ell-2}(kr) - \frac{(\ell + 1)(\ell + 2)}{(2\ell + 1)(2\ell + 3)} j_{\ell+2}(kr) \right] \quad (21)$$

where $r = r(z)$. In turn, *photo-z* effects are included through the radial selection function $\phi(z)$, as discussed in Sec. 2.1.

Notice however that the expressions in Eqs. (19,20,21) are numerically expensive to evaluate due to the oscillatory behavior of $j_\ell(x)$ for $x \gg 1$. In Appendix B1 we discuss our own approach to perform these integrals, valid at large scales and involving the natural cut-off s_{bao} in Eq. (8).

4 N-BODY SIMULATION AND MOCK SURVEY CATALOGUES

As discussed previously, we aim at developing and testing analytical expressions for the signal, variance and covariance of the angular correlation function $w(\theta)$ against measurements in simulated upcoming photometric surveys.

Hence, in order to have a robust statistics but at the same time be representative of such future surveys we used partitions of a very large N-body simulation, provided by the MICE collaboration⁸, to build survey mocks. The simulation, named MICE7680, tracked the gravitational evolution of 2048³ dark-matter particles within an unprecedented comoving volume of $L_{\text{box}} = 7680 h^{-1}$ Mpc using the **Gadget-2** code (Springel 2005). Initial conditions were set at $z_i = 150$ using the Zeldovich dynamics and assuming a flat LCDM cosmology with parameters $\Omega_m = 0.25$, $\Omega_\Lambda = 0.75$, $\Omega_b = 0.044$ and $h = 0.7$. The spectral tilt was set to $n_s = 0.95$ and the initial amplitude of fluctuations set to yield $\sigma_8 = 0.8$ at $z = 0$. The resulting particle mass was $3.65 \times 10^{12} h^{-1} M_\odot$ (see Fosalba et al. 2008 and Crocce et al. 2010 for further details).

Without loss of generality we next assumed a survey covering a continuous 5000 deg² of sky (i.e. a sky fraction $f_{\text{sky}} = 1/8$), and redshift coverage in the range $0.2 < z < 1.4$. In broad terms, this matches the specifications for DES.

In turn, the fact that redshifts are estimated photometrically implies that much of the “small-scales” radial information is lost. In such scenario the best approach is to study angular clustering in redshift bins of width larger or comparable to the mean photo-*z* error (e.g. Simpson et al. 2009). We thus built photo-*z* survey mocks by extracting spherical shells of varying width from “comoving” outputs of MICE7680. Each shell is restricted to span only one octant in angular size and its radius $\bar{r}(z)$ is set to match the comoving distance to the redshift of the output.

To place the spherical shells within the simulation box-size we defined observers in a regular grid and set the number of grid-points in each direction N_i in order to have none or minimal volume overlap between different mocks (while placing the shells in the positive octant of the observer). Strictly non-overlapping mocks can be achieved by setting the

spacing along two cartesian axis equal to $\bar{r} + \Delta r/2$, while the third to $\sqrt{2\bar{r}\Delta r}$. Thus we defined N_z as the integer part of $L_{\text{box}}/\sqrt{2\bar{r}\Delta r}$, while N_x and N_y as the round-off of $\bar{r} + \Delta r/2$ to its nearest integer⁹. Notice that rounding-off instead of taking the integer part could lead to a slight volume overlap in those directions. However we have explicitly checked that volume overlap never exceeds 1% in any of the mocks.

Note that the very large size of MICE7680 is a critical point in order to have a robust statistics in the whole redshift range of the assumed survey.

In order to have a clearer understanding of the different components of the model we built ensembles of mocks in increasing “layers of reality”. We first selected dark-matter particles directly from real space assuming a radial distribution as expected in DES. We also tested, and dismissed, effects due to biased tracers by repeating this exercise starting from halo catalogues. Next we moved particles to redshift space before doing the selection. Alternatively, we imposed a random radial uncertainty in the position of each particle before selection to mimic photometric error. Finally we imposed the radial distribution in addition to redshift distortions and photometric error to build mocks which are closest to a real survey.

Once the particles were selected we built angular number density maps in the **Healpix** format with $N_{\text{side}} = 256$ (Górski et al. 1999)¹⁰. This N_{side} corresponds to 98304 pixels in 1/8 of sky with an angular resolution of 13.75 arc-min. In this way, and given our mass resolution $m_p = 3.65 \times 10^{12} h^{-1} M_\odot$, we obtained mocks with $\sim 0.1 - 0.5$ galaxies per squared arc-min (depending on the bin-width) in the low redshift bins ($z = 0.3$) and $\sim 1 - 4$ galaxies per squared arc-min at high redshift ($z = 1.1$). Once the density field was pixelized we measured the correlation function using the standard estimator (Barriga & Gaztañaga 2002; Eriksen et al. 2002)

$$\hat{w}(\theta) = \frac{1}{N_{\text{pairs}}} \sum_{ij} \delta_i \delta_j, \quad (22)$$

where $\delta_i = (n_i - \langle n \rangle) / \langle n \rangle$ is the density fluctuations in the i -th pixel and N_{pair} is the number of pixel pairs.

In what follows we give a more detailed discussion of the different cases considered, while Table 1 contains a descriptive summary of the final suite of mock ensembles used throughout this paper.

4.1 Real Space Mocks

Let us start by describing our mocks in real (or configuration) space. To fairly sample the range $0.2 < z < 1.4$ we select comoving outputs of MICE7680 at the redshifts $\bar{z} = 0.3, 0.5, 0.73$ and 1.1. In each output we extract all the particles within spherical shells of radius equal to the

⁸ <http://www.ice.cat/mice>

⁹ Except when we include redshift distortions and/or photometric error where take $N_x = N_y = N_z$ and round off $L_{\text{box}}/r(z_*)$ instead, with z_* the redshift at which the true redshift distribution in Eq. (7) is negligible (see Fig. 2)

¹⁰ <http://healpix.jpl.nasa.gov>

comoving distance to the given redshift. In turn, to be representative of typical photo-z errors we set 4 different bin width for each \bar{z} , namely $\Delta z/(1+z) = 0.03, 0.05, 0.1, 0.15$. The comparison of these 16 mock configurations with the approximate $\sigma_z(z)$ expected for DES (Banerji et al. 2008) is shown in Fig. 1.

Translated to comoving distance these bins range from 100 to $500 h^{-1}$ Mpc in width. These spherical shells are restricted to have right ascension and declination in $0^\circ - 90^\circ$, therefore covering 1/8 of sky. Lastly, by randomly selecting particles within each bin we impose the following radial distribution

$$dN/dz \propto (z/0.5)^2 \exp[-(z/0.5)^{1.5}], \quad (23)$$

which is also what is expected in DES (we thank DES LSS working group for providing this).

The resulting number of mocks depends on \bar{z} and $\Delta z/(1+z)$, but it ranges from tens to thousands, making these set of ensembles very suitable for error studies as well as for testing models and systematics. The top panel of Table 1 includes the main characteristics for 11 of these bins, which are the ones that for concreteness we focus on in this paper, although our conclusions extend to the full set.

4.2 Real Space Mocks for biased tracers

In order to study differential features in the angular clustering of biased tracers as compared to that of dark-matter we also built mocks starting from halo catalogues.

We concentrated in two characteristic redshifts and built mocks in exactly the same manner as described in Sec. 4.1. We note however that from the numerical point of view it is very hard to resolve halos of $10^{12-13} h^{-1} M_\odot$ in a volume as large as the one we are considering here, ~ 450 cubic Gpc/h. Thus, to be able to reproduce the mass-scale of LRG halos we choose poorly resolved halos (or groups) as tracers. Note that, although poorly resolved, these groups have the same clustering amplitude and abundance of real LRG galaxies (Cabr e and Gaztan aga 2009).

At $z = 0.3$ we consider groups of $M > 10^{13} h^{-1} M_\odot$ (i.e. 5 or more particles) and bin width $\Delta z/(1+z) = 0.15$. The spatial abundance of these tracers is $\bar{n} = 1.7 \times 10^{-4} h^3 \text{Mpc}^{-3}$.

At $z = 0.5$ we consider halos with $M > 2 \times 10^{13} h^{-1} M_\odot$ (8 or more particles) with $\bar{n} = 0.49 \times 10^{-4} h^3 \text{Mpc}^{-3}$. With these selections we try to mimic LRG halos of $M \geq 10^{13} h^{-1} M_\odot$. At $z = 0.5$ we also consider cluster mass-scale halos of $M > 10^{14} h^{-1} M_\odot$ (35 particles or more), their abundance given by $\bar{n} = 0.64 \times 10^{-5} h^3 \text{Mpc}^{-3}$.

These mocks are summarized in the second panel of Table 1. We do not consider bins at higher redshifts, as the galaxy bias is expected to be closer to linear and local. In addition, since the linear local bias model holds valid to the extent we are able to investigate, see Sec. 5.2, we will next concentrate on the effects of photo-z and redshift distortions on the matter field itself.

Real Space Mocks					
\bar{z}	$\frac{\Delta z}{(1+z)}$	\bar{r}	Δr	\bar{n}	Mocks
0.3	0.03	845.7	102.65	0.11	1344
0.3	0.10	843.3	342.14	0.33	441
0.3	0.15	839.8	513.20	0.47	392
0.5	0.05	1345.8	178.23	0.48	324
0.5	0.10	1343.2	356.50	0.88	175
0.5	0.15	1338.7	534.83	1.21	150
0.73	0.05	1859.7	181.50	0.92	104
0.73	0.10	1856.5	363.10	1.68	96
0.73	0.15	1851.1	544.88	2.30	80
1.1	0.10	2558.2	360.07	2.60	36
1.1	0.15	2551.9	540.56	3.90	36
Real Space Halo Mocks					
\bar{z}	$\frac{\Delta z}{(1+z)}$	M_{halo}	$bias$	\bar{n}	Mocks
0.3	0.15	10^{13}	2.35	$4.0 \cdot 10^{-4}$	392
0.5	0.10	2×10^{13}	2.95	$3.2 \cdot 10^{-4}$	175
0.5	0.10	10^{14}	4.40	$2.9 \cdot 10^{-4}$	175
Redshift Space Mocks					
\bar{z}	$\frac{\Delta z}{(1+z)}$	$f \equiv \frac{\partial \ln D}{\partial \ln a}$	Mocks		
0.5	0.05	0.705	125		
0.5	0.15	0.705	125		
Photo-z Space Mocks					
\bar{z}	$\frac{\Delta z}{(1+z)}$	σ_z	Mocks		
0.5	0.05	0.06	125		
0.5	0.15	0.06	125		
Photo-z + Redshift Space Mocks					
\bar{z}	$\frac{\Delta z}{(1+z)}$	f	σ_z	Mocks	
0.5	0.05	0.705	0.06	125	
0.5	0.15	0.705	0.06	125	

Table 1. *Suite of Mock catalogues.* Each mock consist of a redshift shell subtending 1/8 of sky at a radial comoving distance and width as listed in the top panel. All mocks corresponds to dark-matter particles (except real space halo mocks) with a radial distribution given in Eq. (23). The mean distance \bar{r} and width Δr are in h^{-1} Mpc. The surface density \bar{n} in particles per square arcmin (and for a given bin is similar for real, redshift and photo-z space). Halo-masses are in $h^{-1} M_\odot$ and D is the ‘‘linear’’ growth factor. The photo-z error σ_z equals $140 h^{-1}$ Mpc for our cosmology. The bias reported was obtained from the ratio of angular correlation functions (see Sec. 5.2, also for associated error bars).

4.3 Redshift Space Mocks

To understand the importance of redshift distortions, and the accuracy of the modeling, we built mocks where we impose the radial distribution in Eq. (23) but displace the particles to redshift space prior to the top-hat selection.

We concentrated in the comoving output of MICE7680 at $z = 0.5$ since this redshift is the typical mean z for upcoming photometric surveys such as DES or PanStarrs. We then identified redshift bins of width $\Delta/(1+z) = 0.05$ (thin) and $\Delta/(1+z) = 0.15$ (thick). In each redshift shell the mapping from real \mathbf{r} to *Redshift Space* positions \mathbf{s} is given by the transformation

$$\mathbf{s} = \mathbf{r} + v_r(1+z)/H(z) \hat{\mathbf{r}} \quad (24)$$

where H is the Hubble parameter and v_r the peculiar velocity of the object along the line of sight from the observer. Therefore given the observer at position \mathbf{r}_0 (the center of the spherical redshift shell) we first find the particle's projected velocity along the l.o.s. to the observer,

$$v_r = \frac{\mathbf{v} \cdot (\mathbf{r} - \mathbf{r}_0)}{|\mathbf{r} - \mathbf{r}_0|}, \quad (25)$$

then displace it by $\delta r = v_r(1+z)/H(z)$ along the l.o.s.,

$$\delta \mathbf{r} = \delta r \frac{(\mathbf{r} - \mathbf{r}_0)}{|\mathbf{r} - \mathbf{r}_0|} \quad (26)$$

and finally do the top-hat selection. In total, we built 125 mocks subtending one octant of angular size for each of these two bin widths (see Table 1).

4.4 Photo-z Space Mocks

Sets of mocks including (Gaussian) *Photo-z* errors were also produced in almost the same manner, except that the displacement along the l.o.s was random with a probability

$$f(\delta r) = \frac{1}{\sqrt{2\pi}\sigma_r} \exp\left[-\frac{\delta r^2}{2\sigma_r^2}\right] \quad (27)$$

where $\sigma_r = \sigma_z c/H(z)$, and σ_z is the survey photometric uncertainty at the given z . We only considered $\sigma_z = 0.06$, which is the nominal value for DES at $z = 0.5$ using the *griz* photometric bands (Banerji et al. 2008) as reproduced our in Fig. 1. This is also the expected photo- z accuracy for the 3π all-sky survey of the Pan-Starrs collaboration (Cai et al. 2009) at this redshift using *grizy* bands alone. In addition, it is the approximately photo- z precision obtained for the optical sample of LRGs selected from the SDSS imaging data (Padmanabhan et al. 2005; Padmanabhan et al. 2007). This is thus a very representative value for σ_z . For our cosmology it translates to an uncertainty in the radial distance of $\sim 140 h^{-1}$ Mpc (see Table 1 for details). Once the photometric error was added we selected the particles using top-hat cuts in *photometric* redshift of width $\Delta z/(1+z) = 0.05$ and 0.15 .

The net effect of selecting a sample according to their photometric redshift, e.g. with a top-hat criteria, is to have a broader distribution of true redshifts of the selected galaxies. This is depicted in Fig. 2 where the solid line corresponds to the standard top-hat selection in true redshift as done in the

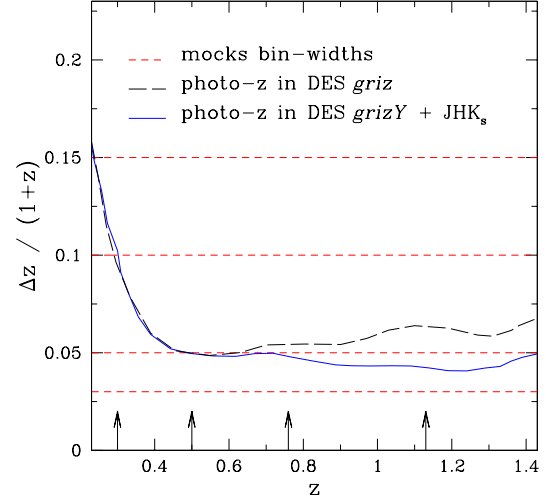


Figure 1. *Mocks configurations* We built several ensembles of mock redshift bins covering $1/8$ of sky (5000 sq deg) and with mean redshifts $\bar{z} = 0.3, 0.5, 0.73, 1.1$ (shown by the inset vertical arrows). For each \bar{z} we set four different redshift width $\Delta z/(1+z) = 0.03, 0.05, 0.1, 0.15$ (dashed lines, bottom to top respectively). A more detailed description of the ensemble of mocks for each configuration is given in Table I. The aim is to resemble with high statistical accuracy the geometry of large area and deep photometry galaxy surveys, such as the Dark Energy Survey (DES). The expected photo- z error in DES (using *griz* bands) is shown by the long dashed line, while the solid line shows the resulting photo- z after adding the JHK_s filters from the Vista Hemisphere Survey (from Banerji et al. 2008).

previous mocks. Dashed line shows instead the true distribution of objects (i.e. as a function of their true redshifts) that in our photo- z mocks entered the (top-hat) photo- z bins of $\Delta z/(1+z) = 0.15$ (left panel) and $\Delta z/(1+z) = 0.05$ (right panel).

These radial selection functions were obtained from Eq. (7) using the underlying distribution from Eq. (23) (shown by the solid line) and a Gaussian $P(z|z_p)$ of width $\sigma_z = 0.06$, Eq. (27), and have been normalized to unity when integrated over redshift. Their importance lies in the fact that this is all one needs in order to compute the model correlation function, as discussed in Sec. 2. In addition, notice that we have chosen mock bin widths such that $\Delta z \sim \sigma_z$ (i.e. a “narrow bin” of width comparable to the photo- z) or $\Delta z \sim 4\sigma_z$ (a “broad bin”).

4.5 “Survey” Mocks : dNdz, RSD and Photo-z

Finally we built mocks that include all the aforementioned effects: a realistic radial distribution Eq. 23, redshift distortions and photometric redshift with uncertainty $\sigma_z = 0.06$. We again concentrated in the mean redshift $z = 0.5$ and two bins of width $\Delta z/(1+z) = 0.05 \sim \sigma_z$ (“narrow”) and $\Delta z/(1+z) = 0.15 \sim 4 \times \sigma_z$ (“wide”). Therefore, these are the closest to an actual photo- z survey such as DES or PanStarrs.

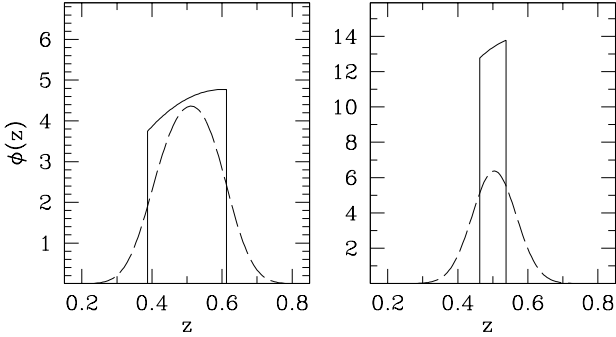


Figure 2. Radial distribution of galaxies vs. true redshift in our redshift distortions and photo- z mocks. Solid lines are the radial distribution of objects for a top-hat selection in true redshift of width $\Delta z/(1+z) = 0.15$ (left panel) and $\Delta z/(1+z) = 0.05$ (right panel), both centered at $z = 0.5$ and assuming a constant spatial density. Dashed lines show instead the distribution of objects as a function of true redshift if the same top-hat selection is now done in photometric redshifts. In this later case a Gaussian photometric redshift error of $\sigma_z = 0.06$ is assumed.

Before moving on we want to stress that our mocks are obtained from *comoving outputs* of an N-body simulation and thus contain all correlations induced by non-linear gravitational evolution as well as projection effects, partial sky coverage and realistic radial selection function. In addition some account for photo- z and/or RSD effects. However, since we do not use *light-cone outputs* they do not include evolutionary effects of the sample within the redshift bin. We argue that, for the narrow bins under consideration, light-cone effects are negligible in front of photo- z and RSD (in the same way nonlinear gravitational effects are, see Sec 5). To leading order, light-cone effects will introduce a *linear* evolution, which can be estimated from Eq. (5) by weighting the selection by the corresponding linear growth (i.e. defined with respect to the mean redshift), $f = D(z, \bar{z}) b(z) \phi(z)$. By doing this, we have found no difference with the same calculation that instead evaluates the growth at the mean redshift of the bin. Nonetheless, this is certainly an interesting subject that needs to be addressed more properly (i.e. with light-cone vs comoving outputs). We leave that for further work.

5 MODEL VS. MOCKS I : THE CORRELATION SIGNAL

In Sec. 2 we discussed in detail our model for the angular correlation function. We now proceed to show how it performs against clustering measurements in the ensembles of mock redshift bins described in Sec. 4.

5.1 Nonlinear Gravity and evolution

Using the model for $\xi(r, z)$ in Eq. (10) we now project into redshift bins according to Eq. (5) to find the angular correla-

tion function. The resulting correlations are shown in Fig. 3 compared with measurements in the mocks at the 4 different mean redshifts, $z = 0.3, 0.5, 0.73, 1.1$ (top to bottom). In each case for a bin width of the size of the typical photometric error achievable at the given redshift in a survey like DES (Banerji et al. 2008).

The agreement between our theoretical model and the mean of the measurements is excellent for all configurations tested, see Table 1, in particular those shown in Fig. 3. And we recall that we are using only two parameters obtained from a best-fit to ξ at $z = 0.3$ ¹¹. Hence the evolution with redshift is a component of the model. In each case displayed error bars correspond to the error on the mean of the ensemble (i.e. $\sigma/\sqrt{N_{\text{mocks}}}$), that given the large number of ensemble member we count on is remarkably small.

The importance of nonlinear effects in front of projection ones are minor if we consider the large error bars achievable in one single mock measurement. It is however encouraging that one is able to model accurately a large range of angular scales, given the mixing of all the distance scales involved in the redshift bin projection. We note that the second term in Eq. (8) does not impact the shape and position of the BAO, but it does bring theory and mocks in better agreement for smaller angular separations.

One interesting result would be to have an estimate of the minimal angle the model is able to reproduce. A conservative approach to investigate this is to match the smaller comoving scale r_s involved in the projection of a galaxy pair subtending an angle θ within a redshift bin (where $r_{\min}(z)$ is the lower limit of the redshift range),

$$r_s = r_{\min}(z)(2 - 2 \cos \theta)^{1/2} \quad (28)$$

with the minimum scale one is capable of modeling in the 3-d clustering.

Interestingly we have found that, if we define r_{nl} as the scale where the model departs from the data by some fixed percentage, then our minimum scale satisfies,

$$r_{nl}(z) \sim r_{nl}(z=0) \times D(z) \quad (29)$$

and $r_{nl}(0) \sim 20 h^{-1} \text{Mpc}$ for a 15% error in ξ . This ensures the following minimal angles above which the model should perform well for the 4 cases shown in Fig. 3, $\theta_{\min} = 1.3^\circ, 0.7^\circ, 0.5^\circ, 0.4^\circ$, in agreement with Fig. 3. But again, this is a conservative limit because the relative contribution of scales $\sim r_s$ to the full redshift bin projection is minor.

5.2 Biased tracers

We now revisit to what extent the possible presence of scale dependent bias in the spatial correlation function of tracers (Smith et al. 2008; Manera and Gaztanāga 2009; Desjacques and Sheth 2010; Desjacques et al. 2010) translates into the angular correlation function, depending on the bin-width and mean redshift. Or equivalently, to what extent the assumption of linear bias holds in the angular clustering

¹¹ The level of matching does not change if we use instead the theoretical expectations for these parameter discussed in Sec. 2.2

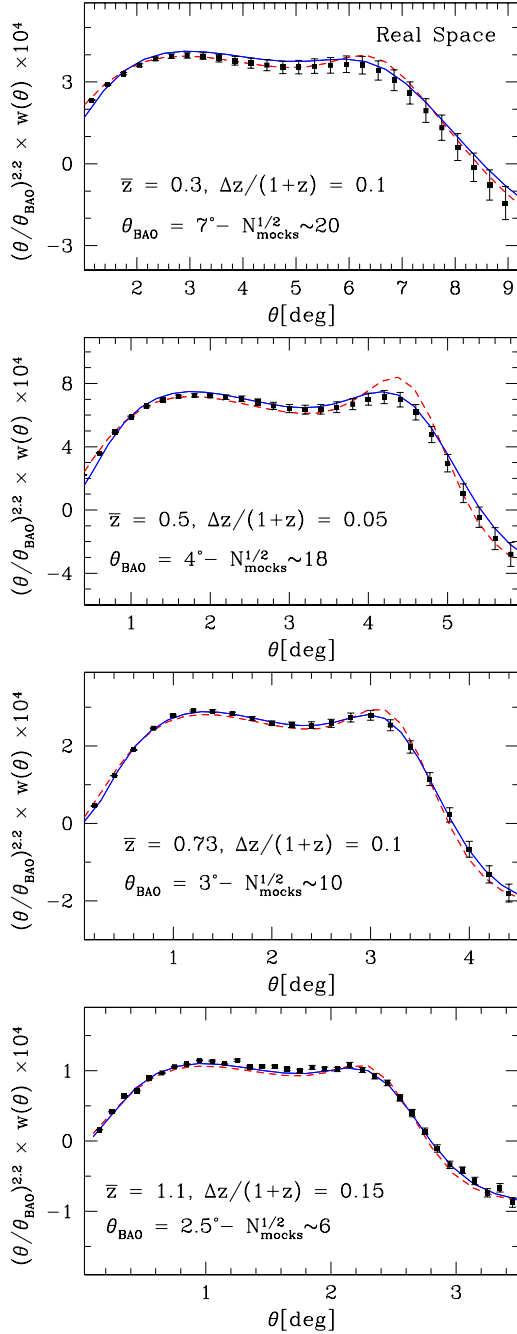


Figure 3. Angular Correlation Function measured in 4 ensembles of mocks z-bins in *Real Space* compared with our nonlinear model (solid blue) and linear theory (red dashed line). Error bars correspond to the uncertainty in the mean, the actual r.m.s. is $N_{mock}^{1/2}$ larger (which is specified in the inset label). We have explored many more configurations than those shown (see details in Table 1 and Sec. 4.1) and the same level of agreement was found.

of halos. For this exercise we thus use the suite of mocks described in Sec. 4.2.

The top panel of Fig. 4 shows the ratio of correlation functions (i.e. the bias) measured in the 392 mocks of $z = 0.3$ and $\Delta z/(1+z) = 0.15$ for halos $M > 10^{13} h^{-1} M_{\odot}$. Middle and bottom panels shows the same ratio but from the 175 mocks bins at $z = 0.5$ and $\Delta z/(1+z) = 0.1$ for masses $M > 2 \times 10^{13} h^{-1} M_{\odot}$ and $M > 10^{14} h^{-1} M_{\odot}$ respectively. For reference the vertical blue arrow shows the position of the BAO peak in each case.

In all cases the bias is scale independent well within error bars (corresponding to the standard deviation of the mean of the ensemble) and at the 2 – 3% level for the cases mimicking galaxy clustering ($M \sim 10^{13} h^{-1} M_{\odot}$). For cluster mass-scale the shot-noise of the sample is much larger and consequently so the error bars. Nonetheless, there is not clear tendency with scale. We recall that our galaxy-type halos are poorly resolved. However we have found that increasing the resolution (i.e. the minimum number of particles per halo) and so the typical halo-mass, does not alter the scale independence of the bias shown in the top panels of Fig. 4.

The error bars displayed in the top and middle panels of Fig. (4) were obtained from the r.m.s of the mocks and correspond to the mean of the ensemble.

For cluster mass-scale halos (bottom panel) it was not possible to obtain the bias ratio $(w_{hh}(\theta)/w(\theta))^{1/2}$ for every single mock and angular separation due to the large shot-noise dominated errors that led to $w_{hh} < 0$ in some cases. We have then estimated the bias as $(\langle w_{hh} \rangle / \langle w \rangle)^{1/2}$ and the errors propagating the r.m.s. ensemble errors in the halo angular auto-correlation w_{hh} and the matter angular auto-correlation w as,

$$\delta b/b = (1/2) [(\delta w_{hh}/w_{hh})^2 + (\delta w/w)^2]^{1/2} \quad (30)$$

and converting to errors on the mean by $\delta b \rightarrow \delta b/\sqrt{N_{mocks}}$. We have tested using the lower mass-scale halos that this approach of the purely ensemble average leads to the same bias and errors.

In summary, we conclude that there is no evidence of scale dependent bias for these tracers within the error bars.

5.3 Redshift Distortions and Photo-z

Let us now discuss the impact of redshift distortions and photometric errors in $w(\theta)$. Figure 5 corresponds to the angular correlation measured in the mocks in configuration space from Sec. 4.1 (middle green symbols), redshift space from Sec. 4.3 (top red symbols) and photo-z space from Sec. 4.4 (low blue symbols). In solid green, red and blue lines we show the corresponding analytical predictions obtained from Eqs. (5,7,10,B8). Black dashed line and symbols depict the model and measurements when accounting for all effects at once, with mocks introduced in Sec. 4.5. For redshift distortions we used that $\beta = f(z = 0.5) = 0.7047$ for our cosmology (since $b = 1$) while for photo-z we used the selection functions shown in Fig. 2.

Error bars displayed in Fig. 5 are true ensemble errors corresponding to the standard deviation of the mean (i.e.

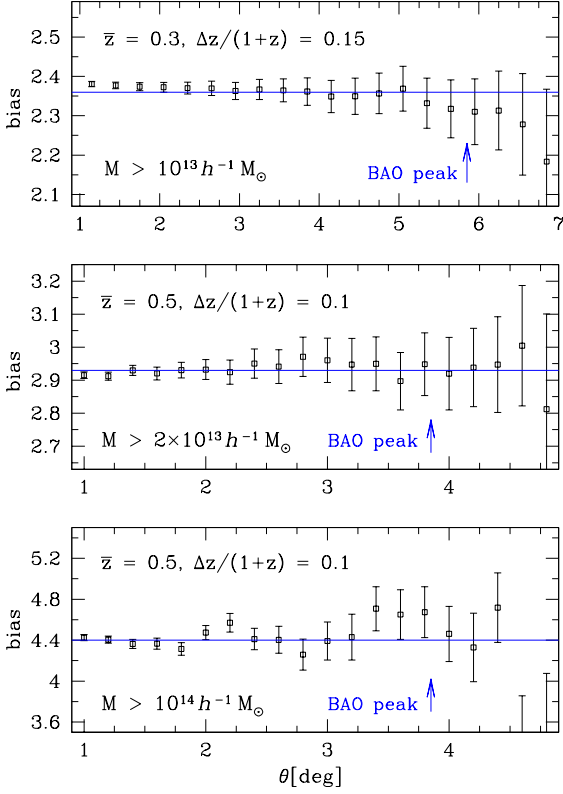


Figure 4. Large Scale Halo Bias (Real Space), in the angular correlation function for bins at $z = 0.3$ (top panel) and $z = 0.5$ (middle and bottom). The bias is linear within few percent, and well within error bars. Except perhaps in the lower panel, that corresponds to cluster-scale mass halos with large errors fully dominated by their low abundance. See text for more details.

$\sigma/\sqrt{N_{mocks}}$, where σ is the r.m.s variance of $w(\theta)$ measurements). They increase from $\sim 1\% - 2\%$ at 2° to $\sim 3\% - 4\%$ at 4° (the angular BAO scale). Hence, Fig. 5 clearly shows that the model described in this paper performs remarkably well for both thin and thick bins, in configuration, redshift, and/or photo-z spaces. In redshift space it tends to underestimate the measurements for $\theta < 3^\circ$ at the $\sim 2\%$ level.

Redshift space distortions produce a strong enhancement of the clustering signal (see (Nock et al. 2010) who find similar results for the projected correlation). This effect is also a strong function of scale, becoming more important for larger separations. Indeed, it increases the amplitude of the BAO bump by as much as a factor of 2.3 for the thin bin of $\Delta = 0.05(1+z) \sim 180 h^{-1} \text{Mpc}$ (top panel of Fig. 5) and 1.5 for the thick one of $\Delta = 0.15(1+z) \sim 530 h^{-1} \text{Mpc}$ (bottom panel of Fig. 5).

In turn, photo-z errors have the opposite effect to that of redshift distortions, decreasing the overall amplitude of angular correlations. This is simply because the projection in Eq. (5) extends over a much larger range of scales (e.g. see Fig. 2). Notably, this effect is not far from being scale independent. For the thin bin the impact is a bit stronger (top panel of Fig. 5). If we only consider photo-z effects, the

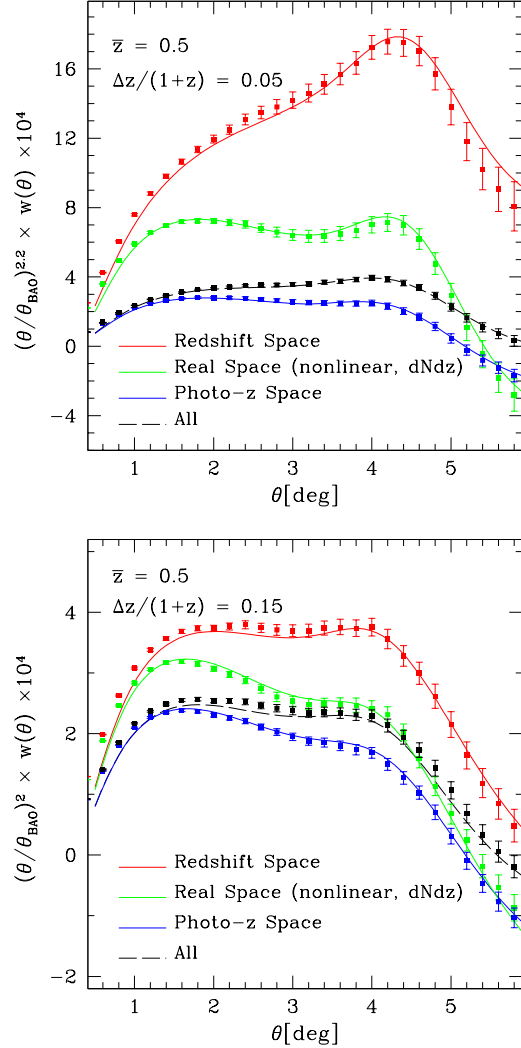


Figure 5. Redshift Distortions vs. Photo-z effects: We show the mean correlation over 125 mock measurements, and the corresponding predictions, in configuration (middle green line and symbols), redshift (top red line and symbols) and photo-z space (low blue line and symbols). Black line and symbols corresponds to mocks measurements and model when all effects are combined together. Redshift distortions (RD) depend on the parameter $\beta = f/b = 0.7047$ in our cosmology, while photo-z errors were set to $\sigma_z = 0.06$. Hence, top panel corresponds to a bin of width $\Delta z \sim \sigma_z$ while bottom to $\Delta z \sim 4 \sigma_z$. RD induces a strong and scale dependent enhancement of the correlation, counteracted by the smearing due to the photo-z uncertainties. Error bars shown correspond to the standard deviation of the mean of the ensemble.

amplitude of $w(\theta)$ decreases by $\sim 60\%$ when going from true to photometric redshifts (green to blue lines in the figure). In the case of a wide bin (bottom panel in Fig. 5), although its width is approximately 4 times the photo-z there is still a reduction in amplitude of $\sim 30\%$.

The total angular correlation, including redshift distortions, photo-z, nonlinear evolution and bin projection effects is depicted by the dashed line in Fig. 5. In the case of bin

width comparable to the photo- z error the effect of photo- z dominates over redshift distortions (even though the impact of redshift distortions is larger for thinner bins). For a wider bin (bottom panel) the conjunction of effects leaves the amplitude of correlation at the BAO peak almost unchanged, but it does introduce a strong scale dependent bias with respect to the real space clustering. Notably, the inclusion of redshift distortions to the $w(\theta)$ in photo- z space enhances the amplitude by up to 50% at the peak position. Clearly, the appropriate inclusion of these contributions can be crucial in the analysis of real data.

We note that the above conclusions assume an unbiased tracer. For biased ones the impact of redshift distortions, sensitive to f/b , is smaller. For instance, if we take $b = 1.7$ at $z = 0.5$, that is a characteristic value for optically selected LRGs (Padmanabhan et al. 2007; Ross et al. 2007), but keep the same σ_z we find the amplitude of $w(\theta)$ at the BAO peak position ($\theta \sim 4^\circ$) reduced by $\sim 10\%$ with respect to the $b = 1$ case, for a bin $\Delta \sim 4 \times \sigma_z$ (but still gives 30% boost with respect to the case where redshift distortions is neglected all together). This, of course, might or not be accompanied by a corresponding change in the amplitude of errors depending on whether the galaxy sample is shot-noise dominated or not.

5.4 Dependence on redshift distribution

The very good match shown so far between the model correlation and the mock measurements relies in the fact that we have a perfect knowledge of the true redshift distribution. However when analyzing real data this can only be true to a certain extent. This is particularly so for photometric data, where different photo- z codes assign different redshift estimates to the same galaxies and thus could lead to slightly distinct redshift distributions in each redshift bin (e.g. Abdalla et al. 2008 and references therein). To understand the extent by which the angular correlation is affected by this potential unknown we first fitted the redshift distribution for our narrow top-hat bin in photo- z space (assuming $\sigma_z = 0.06$) with a normal distribution,

$$\phi(z) = \frac{1}{\sqrt{2\pi}\sigma} \exp[-(z - \mu)^2/2\sigma^2]. \quad (31)$$

We found that $\mu = 0.512$ and $\sigma = 0.0628$ leads to an excellent agreement between the analytic expression in Eq. (31) and the exact distribution shown by a dashed line in the right panel of Fig. 2. We next increased μ by 3% and separately σ by 10% and re-computed the angular correlation. These off-sets are similar to the variations recently found by Thomas et al. 2010 when analyzing the photometric sample of LRGs in SDSS with 6 different photo- z codes, and selecting top-hat redshift bins comparable to the one discussed here ($\bar{z} = 0.5$, $\Delta z/(1+z) = 0.05$). As a third example we allowed the center of the redshift distribution to vary as much as the assumed photo- z , to $\mu = 0.572$. The resulting correlations are shown in Fig. 6. We include also the measurements in the corresponding photo- z mocks (already presented by black symbols in top panel of Fig. 5). Error bars shown are the r.m.s variance over the ensemble (rather than variance on the mean) to be representative of a real survey situation.

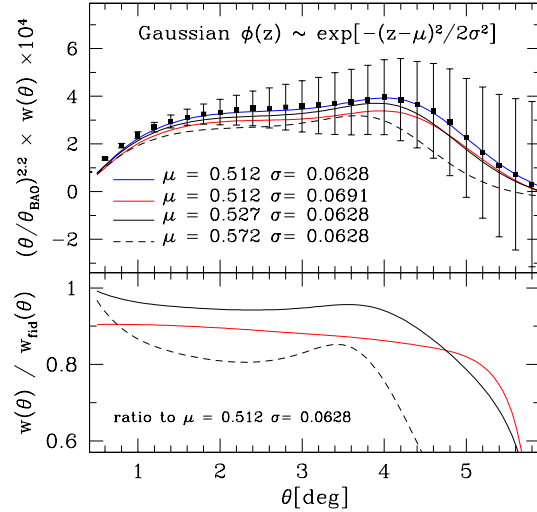


Figure 6. Dependence of $w(\theta)$ on the redshift distribution. Top panel: Solid blue line is the correlation from the “true” distribution modeled as a gaussian of mean $\mu = 0.512$ and variance $\sigma = 0.0628$. Other lines are the model correlation from distributions slightly off this one, as indicated in the labels. Also shown are mock measurements with errors corresponding to a 5000 deg^2 photometric survey with nominal photo- z $\sigma_z = 0.06$. Bottom panel: ratio of the different $w(\theta)$ to the “true” case with $\mu = 0.512$ and $\sigma = 0.0628$. Varying the mean by 3% and 10% leads to shifts in the location of the BAO feature by approximately the same relative amounts (solid and dashed black lines respectively), in addition to changes in the amplitude. Increasing the variance by 10% lowers the correlation by $\sim 10\%$ and introduces a scale dependent modulation of the amplitude but does not affect the peak (solid red line).

As noticeable in the figure variations in μ and σ lead to analogous variations in $w(\theta)$. Incrementing the width of the distribution by $\sim 10\%$ reduces the amplitude of the correlation function by about 10% and introduces a scale dependent bias across all the angular range (see bottom panel). In turn, displacements in the mean redshift of the radial distribution shifts the angular position of the BAO peak by comparable percentage amounts (this is more evident when shifting μ by 10%, see dashed line in Fig 6), in addition to the amplitude. If we instead lower μ or σ the effects persist but are reversed.

The main conclusion is that a poor knowledge of the true distribution (e.g. from uncertain photometric estimates) can lead to serious systematic effects depending on the statistical errors of the survey under consideration.

6 MODEL VS. MOCKS II : THE ERROR MATRIX

We now move to test the performance of Eq. (18) in evaluating the full covariance matrix in $w(\theta)$ measurements. We first discuss the diagonal component, or variance, in Sec. 6.1 and then the reduced covariance in Sec. 6.2.

6.1 Comparing the $w(\theta)$ variance

In Fig. 7 we show the r.m.s variance resulting from $w(\theta)$ measurements in several ensembles of mock redshift bins in *Real Space* (top panels corresponds to *narrow* bin cases, bottom to their *wide* counterpart). The bin selection was top-hat in true redshift. The total number of mocks in each ensemble depends on the particular value of mean redshift and width of the bin (as detailed in Table 1), but they are mostly over few hundreds, thus giving a unique statistical framework for our analysis. Solid lines in Fig. 7 corresponds to the prediction for the error,

$$\Delta w(\theta) \equiv \text{Cov}(\theta, \theta)^{1/2}, \quad (32)$$

from Eq. (14) using either $C_{\ell, \text{Exact}}$ (solid blue) or $C_{\ell, \text{Limber}}$ (solid red). The agreement between the theory and mocks is remarkably good for all the range in θ of interest for large scale structure studies, in particular BAO, and all bin configurations. As we move to higher redshifts / wider bins the statistics becomes slightly poorer, but the agreement is still evident. In turn, the Limber approximation over-estimates the error by as much 30% for thin bins but it rapidly converges to the exact result for bins wider than $\sim 200 h^{-1} \text{Mpc}$ (e.g. the cases $\bar{z} = 0.3 - \Delta z/(1+z) = 0.15$ or $\bar{z} = 0.5 - \Delta z/(1+z) = 0.15$, at the bottom left panels).

Let us now discuss the prediction of errors including photo- z effects and redshift space distortions. The left panel of Fig. 8 shows the r.m.s variance in the 125 mocks that incorporate photometric redshift uncertainties as described in Sec. 2.1. The mean redshift was $\bar{z} = 0.5$ and the photo- z error assumed was $\sigma_z = 0.06$ (Gaussianly distributed). Note that in this case, the selection was top-hat in *photo- z* space. The true redshift distribution of objects used in modeling of C_ℓ (as detailed in Eqs. (19-20) and Appendix B1) is given in Fig. 2.

We considered two characteristic *photometric* redshift bin widths, one comparable to the photo- z error ($\Delta = 0.075$), and one almost 4 times larger ($\Delta = 0.225$). In both cases the prediction in Eqs. (19-20), shown by solid blue and dashed red lines, is in very good agreement with the mock measurements (in empty and filled symbols).

The middle panel of Fig. 8 shows instead the r.m.s error obtained from the same bins in redshift space. The prediction, in Eqs. (19-20-21), works to good accuracy in this case as well, for both wide and thin redshift widths. Notice that in the cases shown in this section the error is “sampling variance” dominated (i.e. negligible shot-noise), and therefore is expected to scale with the signal itself. This is reflected in Figs. 7 and 8 where in photo- z space the r.m.s error is smaller than in real space, and viceversa for redshift space. In addition, there are some wiggly features in the measurements not reproduced by the model. These, we believe, are due to an insufficient number of mocks (as they also show up in Fig. 7 for ensembles with similar number of mocks).

The right panel of Fig. 8 show the error measured in our most realistic 125 mocks including both photo- z and redshift distortions. They resemble (in amplitude) those in photo- z space indicating that the spreading of the galaxy distribution due to photometric uncertainties is the dominant effect in front of redshift distortions for these redshift bins.

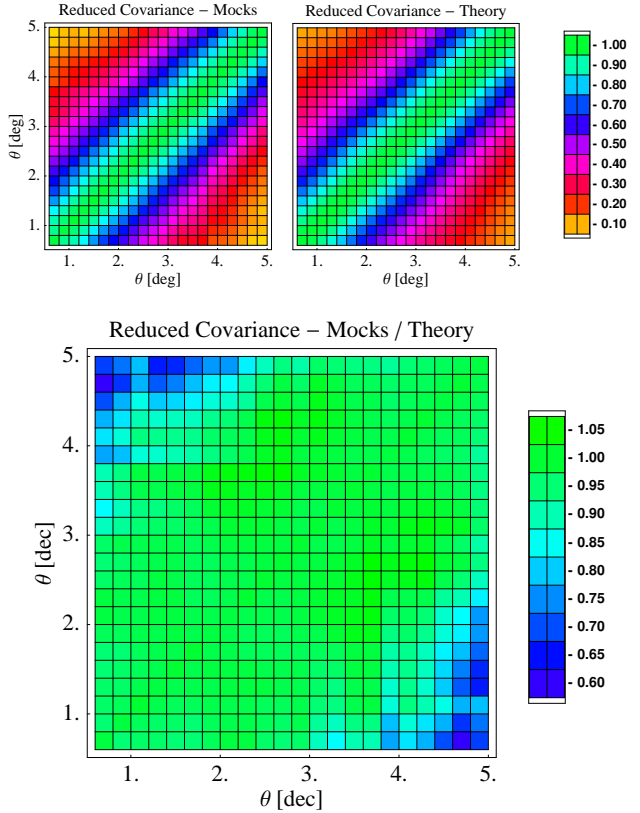


Figure 9. Measured Reduced Covariance Matrix (top left) vs. the Model in Eq. (18) (top right) for the bin centered at $\bar{z} = 0.5$ and width $\Delta z/(1+z) = 0.05$ in Real Space. Bottom panel shows their ratio. Notably, the agreement is within 5% for most of the reduced covariance. The largest differences arise in areas far from the diagonal where the reduced covariance is close to zero anyway.

6.2 Comparing the $w(\theta)$ reduced covariance

Once the diagonal error is well modeled we can turn to the prediction of the full (reduced) covariance matrix. We will concentrate in mocks that are “sampling variance” dominated, in real and redshift plus photo- z space and leave the case of “shot-noise” dominated error to Sec. 6.3.

Figure 9 shows the reduced covariance matrix, $\text{Cov}_{\text{Reduced}}(\theta, \theta') \equiv \text{Cov}(\theta, \theta')/\Delta w(\theta)\Delta w(\theta')$, measured in 324 mocks in Real Space at $\bar{z} = 0.5 - \Delta z/(1+z) = 0.05$ (top left panel). The corresponding model from Eq. (18) is depicted in the top right panel. Bottom panel shows the ratio of mock measurements to model. Remarkably they agree with each other within $\sim 5\%$ for the majority of elements, with the largest differences arising in areas far from the diagonal where the covariance is small anyway.

In order to make a more quantitative evaluation of our analytical expressions we instead plot in Fig. 10 four rows of the reduced covariance matrix, that is, the correlation between $w(\theta)$ and $w(\theta')$ as a function of θ' (at fixed values of θ , as labeled in the plot). We have chosen to do this at our four mean redshifts, $z = 0.3, 0.5, 0.73, 1.1$ and characteristic widths 0.15, 0.1, 0.1, 0.15 respectively (from top to bottom). This election reflects the fact that the calibration

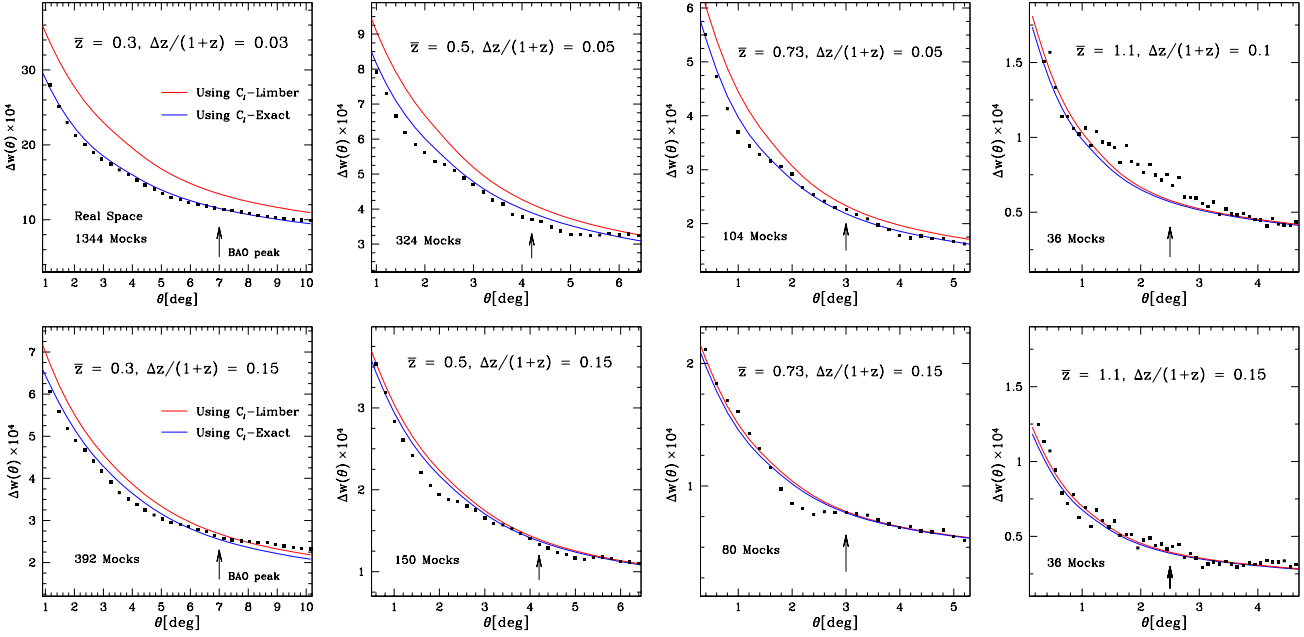


Figure 7. Error in the Angular Correlation Function in Real Space. Predictions for $\Delta w(\theta) \equiv \text{Cov}(\theta, \theta)^{1/2}$ from Eq. (18) using either the exact integration for C_ℓ (blue solid line) or the Limber approximation (red solid line). Symbols are the r.m.s dispersion in measurements of $w(\theta)$ in our ensembles of mock redshift bins in real space (see Sec. 4.1 and top panel of Table 1). Top panels show thin bins and bottom their wide counter-case. Notice that even as many as 100 mocks can still show sample variance fluctuations in the determination of the error.

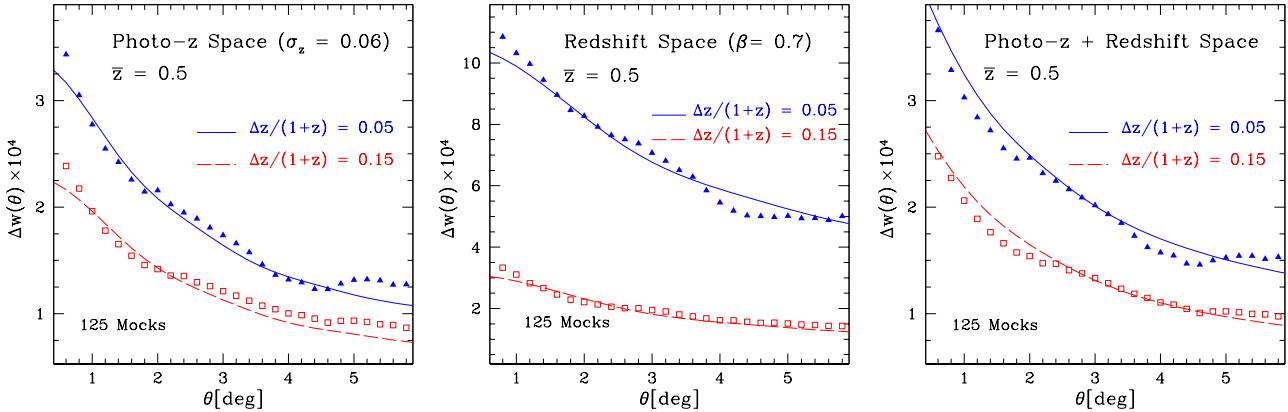


Figure 8. Errors in $w(\theta)$ including photo- z and redshift distortions effects. Left panel shows the r.m.s variance in measurements of $w(\theta)$ in two top-hat redshift bins in photo- z space, both centered at (photometric) $\bar{z} = 0.5$. The assumed photometric error is $\sigma_z = 0.06$. Central panel shows the same quantities measured in redshift space (i.e. top-hat selection is done in true redshift). Right panel incorporates both effects, redshift distortions and photometric errors. The corresponding analytic predictions are given by the solid and dashed lines. In each panel, empty squares corresponds to a “narrow” bin ($\Delta z \sim \sigma_z$) and filled triangles to a “broad” one ($\Delta z \sim 4\sigma_z$).

of photometric redshifts (mimicked here by the bin width) are better at intermediate redshift, and worse towards low and high z . Solid lines in Fig. 10 are the predictions from Eq. (18) using C_ℓ from Eq. (B5).

In all cases, the values of θ' were selected in such a way to span the whole angular regime where the analytical model for $w(\theta)$ is accurate. In particular, the third from the

left value of θ' corresponds approximately to the angular position of the BAO peak

This figure reflects the high degree of correlation between θ -bins even when widely separated, which is characteristics of Configuration space. Nonetheless the theoretical estimates accounts for the whole shape, particularly close to the diagonal. Away from it there are wiggly features in

the measurements that we identify with an insufficient number of mocks (e.g. only the upper panel with ~ 400 mocks does not show these features). The bottom panel shows an extreme case of using only ~ 40 mocks, and the associated level of noise.

Figure 11 shows the same quantity now measured in our mocks including photo- z ($\sigma_z = 0.06$) and redshift distortions effects ($\beta = 0.70$). Here the modeling, which follows from Eqs. (19,20,21,B5) Eq, works remarkably well close to the diagonal. Away from it, at angular separations of $\theta \sim 2 - 1.5^\circ$, we see that the model under-estimates the reduced covariance. This is more noticeable when the reduce covariance drops 0.5. This could be due to shortcomings of the theoretical model or to an insufficient number of mocks. Nonetheless, we have checked that this difference does not translate into different estimates of cosmological parameters when using the theoretical or ensemble covariance matrix. This will be presented in a forthcoming paper (Ross et al. 2010).

Figure. 12 shows instead the off-diagonal elements of the error matrix $\text{Cov}(\theta, \theta + \Delta\theta)$ for fixed value of $\Delta\theta$, and as a function of θ . Top panels correspond to two bins in real space (as labeled) while bottom panels to our mocks in photo- z + redshift space at $\bar{z} = 0.5$ and $\Delta z/(1+z) = 0.015$ (left) or 0.05 (right). The value of $\Delta\theta$ was chosen to sample the full angular width of the BAO feature. In all, the model performs quite well, with no general or obvious systematic deviations. It gives accurate results close to the diagonal (i.e. smallest $\Delta\theta$) and can deviate by $\sim 10\% - 20\%$ for large $\Delta\theta$ (in a regime where covariance is noisy nonetheless).

We finish this section comparing theory and mocks at the level of the Singular Value Decomposition (SVD) to illustrate how well we can model the covariance matrix in a different basis, one which is sometimes used to analyze real data. The top panel of Fig. 13 shows the Singular values of the covariance matrix measured in the ensemble of 392 mocks with $\bar{z} = 0.5 - \Delta z/(1+z) = 0.15$. For the SVD we used a range of scales $[0.25^\circ - 8^\circ]$, divided in 34 bins of width 0.3° (but results are robust for other ranges and binnings). The analytical model, using the linear power spectrum (solid blue line), describe accurately 10 to 15 singular values. We have tested that using more than 10 or 15 singular values the estimate of cosmological parameters have negligible impact in the outcome (see also (Eisenstein & Zaldarriaga 2001)), as they describe very short-range correlations (see bottom panel). These results will be presented in a forthcoming paper (Cabr e et al. 2010). There is however, a simple way to improve on the agreement. In dashed line we show the results when using the ‘‘measured’’ C_ℓ spectra in Eq. (18)¹². This indicates that the recovery of these high singular values is affected by the high ℓ tail of C_ℓ where non-linear effects increase the power over their linear value. On the one hand this will have little importance in practical situations where this regime will be most probably dominated by shot-noise. On the other hand it can be easily modeled using fits to the nonlinear power spectrum, such as **halofit**, into the Limber

¹² We used the publicly available **SpICE** code (Szapudi et al. 2001) to measure the C_ℓ spectra, which is particularly suitable to include mask effects due to partial sky coverage

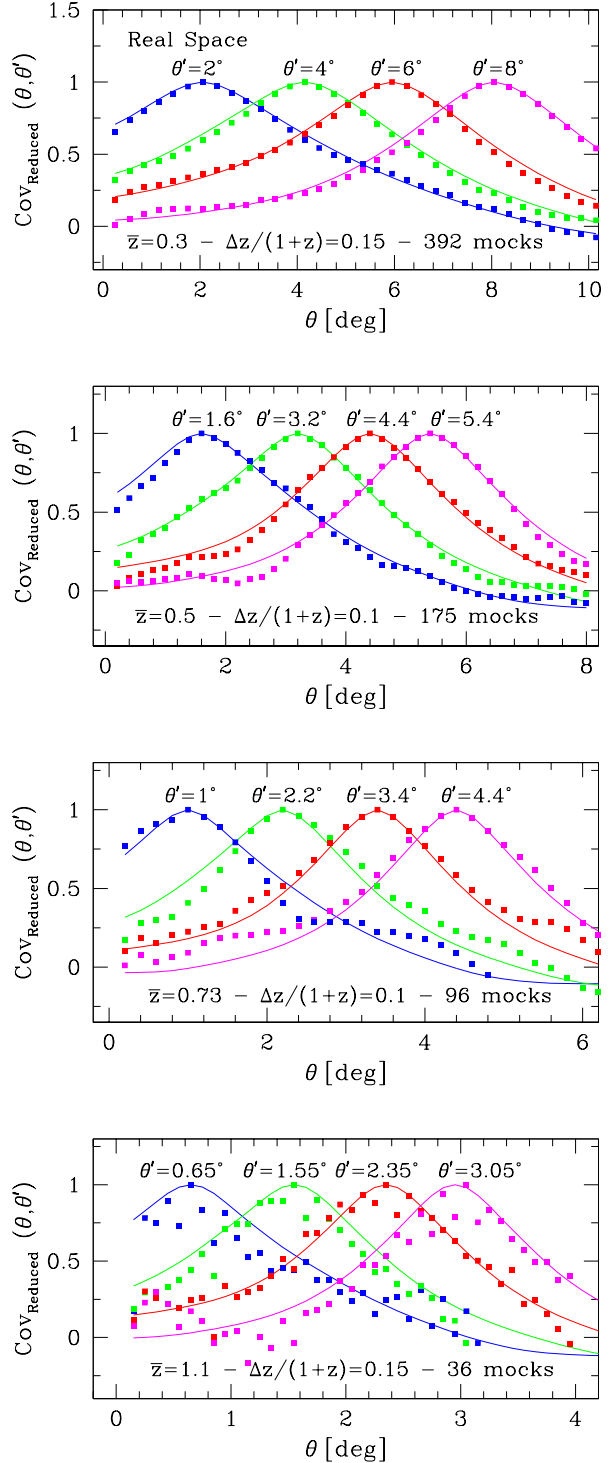


Figure 10. Rows of the Reduced Covariance Matrix in Real Space. Reduced covariance between $\hat{w}(\theta)$ and $\hat{w}(\theta')$ for a fixed value of θ' . From top to bottom we show bin configurations with larger width at low and high redshifts and smaller at intermediate values (resembling the characteristic performance of photo- z estimates). Solid lines are the predictions from Eq. (18). Notice that close to 200 mocks are necessary for a robust estimation of the covariance. In each panel the third from left value of θ' corresponds to the angular BAO scale.

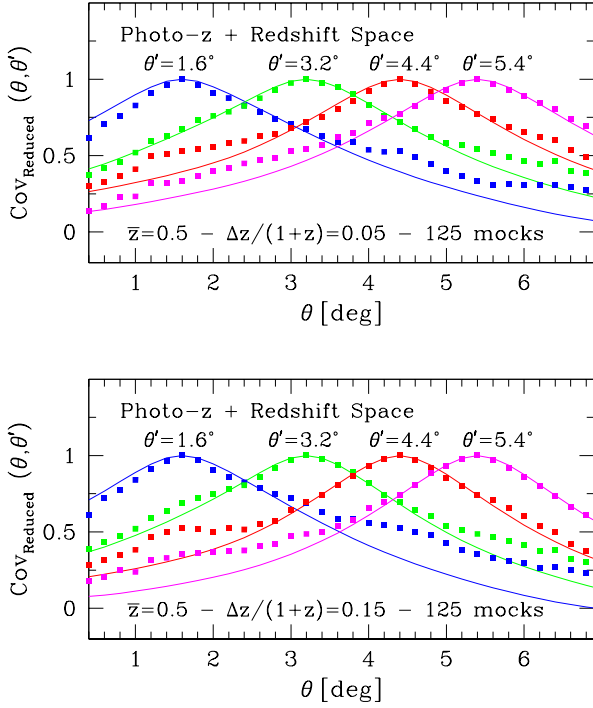


Figure 11. Same as Fig. 9, but for $w(\theta)$ measured in mocks including photo- z and redshift distortions effects. Top panel corresponds to a top-hat bin of width $\Delta z/(1+z) = 0.05$ centered at (photometric) $\bar{z} = 0.5$, while bottom panel to $\Delta z/(1+z) = 0.15$.

formula. In the bottom panel of Fig. 13 we show the singular vectors corresponding to singular values 1, 3 and 6.

So far we have not tested our model against measurements of $w(\theta)$ covariance between different redshift bins. The full covariance matrix in this case can be easily obtained with the same formalism described in Sec. 3 with the full sky variance of C_ℓ^{ij} spectra between bins i and j given by,

$$\text{Var}(C_\ell^{ij}) = \frac{1}{2\ell+1} [(C_\ell^i + n_i)(C_\ell^j + n_j) + (C_\ell^{ij})^2] \quad (33)$$

what leads to (for partial sky coverage),

$$\text{Cov}_{\theta\theta'}^{ij} = \frac{1}{f_{\text{sky}}} \sum_{\ell \geq 0} \frac{2\ell+1}{(4\pi)^2} P_\ell(\cos \theta) P_\ell(\cos \theta') \left[(C_\ell^i + n_i) (C_\ell^j + n_j) + (C_\ell^{ij})^2 \right] \quad (34)$$

Here C_ℓ^{ij} is obtained by simply replacing $\Psi_\ell^2 \rightarrow \Psi_{i,\ell} \Psi_{j,\ell}$ in Eq. (19), where Ψ_i is given by Eq. (20) with the radial selection corresponding to the i -th redshift bin.

6.3 The impact of shot-noise

Previous sections showed that the expression in Eq. (18) can describe remarkably well the error due to *sampling variance* in the measurement of the angular correlation function in redshift bins.

We now turn into the problem of describing the error

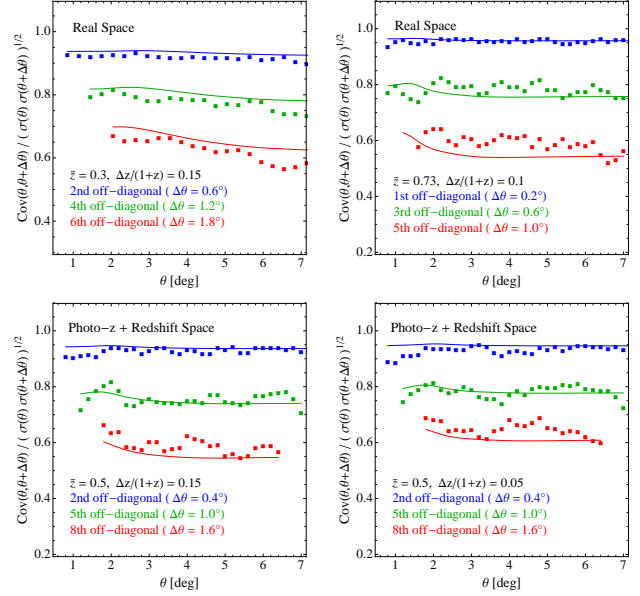


Figure 12. Off-diagonal Covariance in Real Space (Top Panels) and in Redshift + Photo- z Space (Bottom Panels). Panels show the reduced covariance matrix between $w(\theta)$ and $w(\theta + \Delta\theta)$ for increasing values of θ and fixed $\Delta\theta$. Mean red-shift and width of each bin configuration are labeled in the plot. Solid lines are the predictions from Eq. (18) while symbols denote measurements in the corresponding mocks.

due to shot-noise. To this end we will concentrate on different halo samples as tracers (from Sec. 5.2) and test whether the standard Poisson shot-noise term in Eq. (18) can account for the increase in errors due to their low number density.

For concreteness we focus on two characteristic z -bin configurations. Figure 14 corresponds to halos with $M \geq 10^{13} h^{-1} M_\odot$ in the bin at $\bar{z} = 0.3$ and width $\Delta z/(1+z) = 0.15$. This sample has a bias $b(z = 0.3) = 2.36$ (see Fig. 4), what corresponds to $b \sim 2$ if linearly evolved to $z = 0$ (Fry 1996). The sample has an angular abundance of $N/\Omega \sim 17$ halos/deg² what gives a shot-noise contribution, Ω/N , of order $1.8 \times 10^{-5} \text{sr}^2$. This corresponds to $\bar{n} b^2 C_\ell \sim 1$ at $\ell \sim 200$.

Top panel of Fig. 14 shows the r.m.s. error measured in the ensemble of 392 mock redshift bins while lines are the predictions from Eq. (18) using the exact C_ℓ integration and including Poisson shot-noise (solid blue) or neglecting it (dashed blue). As we see the presence of shot-noise increases the error by 20% (in this case), but this can be very well modeled by the addition of the simple Poisson shot-noise $1/\bar{n}$ contribution to C_ℓ . Bottom panel shows the singular values of the covariance matrix SVD. Almost none of the singular values is well recovered when shot-noise is neglected.

In turn, Fig. 15 corresponds to halos with $M \geq 2 \times 10^{13} h^{-1} M_\odot$ at higher redshift, in the bin $\bar{z} = 0.5 - \Delta z/(1+z) = 0.1$ (the halo mass-cut was chosen slightly higher at higher redshift to resemble a flux-limited survey). In this case the bias is $b(z = 0.5) = 2.93$ ($b \sim 2.3$ at $z = 0$) with an angular abundance of ~ 11 halos/deg² ($\bar{n} b^2 C_\ell \sim 1$ at

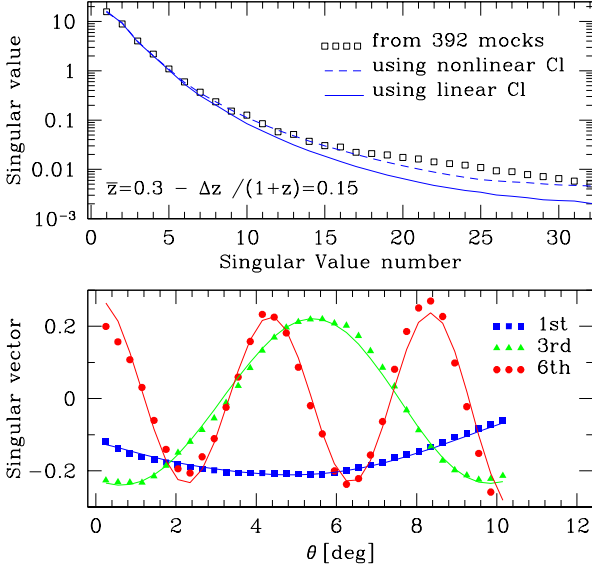


Figure 13. *Singular Value Decomposition* of the Error Matrix measured in 392 mocks at $z = 0.5 - \Delta z / (1+z) = 0.15$. Using the linear power spectrum is possible to reproduce very accurately ~ 15 singular values (top panel) and their singular vectors (bottom panel). Including nonlinear clustering effects into C_ℓ leads to a good match for all singular values. The case shown corresponds to unbiased tracers and negligible shot-noise.

$\ell \sim 200$). The shot-noise increases the error by $\sim 30\%$ on top of the sampling variance (solid vs. dashed lines in the top panel) and plays a crucial role in the SVD eigenvalues (bottom panel). For this case the SVD was done using 40 bins of width 0.2° in the range $[0.2^\circ - 8^\circ]$.

Remarkably, in both cases (Figs. 14 and 15), the inclusion of the simple Poisson white-noise on top of the sampling variance in Eq. (18) accounts very well for all singular values as well as the diagonal error (solid lines).

Arguably, the halo samples used in this test are too much dominated by shot-noise. We have also done the exercise of gradually increasing the relative contribution of shot-noise in front of sampling variance by increasingly under-sampling the dark matter field. As expected, the error is always recovered by the model just by increasing the Poisson term in Eq. (18) accordingly.

6.4 Independence on bin-size

When estimating a covariance matrix one important issue to be considered is whether the binning used for the measurements have an impact on the recovered correlations. Hence, in this section we aim at showing that our estimates for the covariance matrix are not affected by simple rebinning of the measurements, and so our model remains applicable in a general sense.

The selection of bin size, and binning strategy (e.g. linear vs. logarithmic), is particularly important when analyzing real data because one might be able to optimize the

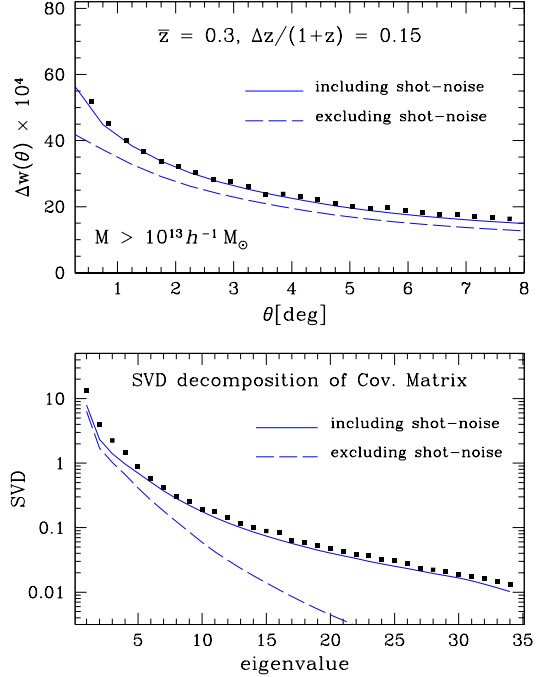


Figure 14. *The effect of shot-noise at $z = 0.3$.* Diagonal error (top panel) and Singular Value Decomposition of the Covariance Matrix (bottom panel) for the bin $z = 0.3$ and $\Delta z / (1+z) = 0.15$ for a sample of halos with $M > \times 10^{13} h^{-1} M_\odot$. The (Poisson) shot-noise term increases the error by $\sim 20\%$ on top of sampling variance (solid and dashed lines are the model with and without the $1/\bar{n}$ term) and is critical to recover the correct singular eigenvalues. We used 392 mocks for this case.

recovered model constrains by a better split between true signal from noise. This is not our goal but still is appropriate to discuss our binning choices.

In general, a too narrow bin could lead to noisy (due to shot-noise in the bin) and very correlated errors. Too wide would smooth and “diagonalize” the covariance but at the expense of leaving only few data points where to compare with the model. In turn, a logarithmic instead of linear binning is preferably when dealing with a large dynamic range in scales. For the problem considered in this paper, the angular correlation at large scales, we are never beyond a factor of 10 in dynamic range in θ , see for instance Fig. 3. In turn we want to sample this range uniformly, which inclined ourselves to linear binning.

In addition, since we have a feature in our signal that we want to resolve (the BAO bump) we need several bins across it which sets our maximum bin-size. We then chose to have $\sim 5 - 10$ bins across it which led to $\Delta\theta = 0.3^\circ$ at $z = 0.3$, $\Delta\theta = 0.2^\circ$ at $z = 0.5 - 0.73$ and $\Delta\theta = 0.1^\circ$ at $z = 1.1$. Still, we could have selected thinner bins.

Therefore, in Fig. 16 we show the measured diagonal error and the reduced covariance (i.e. same as Figs. 7 and 10) for the mock configuration centered at $\bar{z} = 0.73$ (in real space) for a bin-size half the one used throughout the paper. Top two panels correspond to the diagonal error while bot-

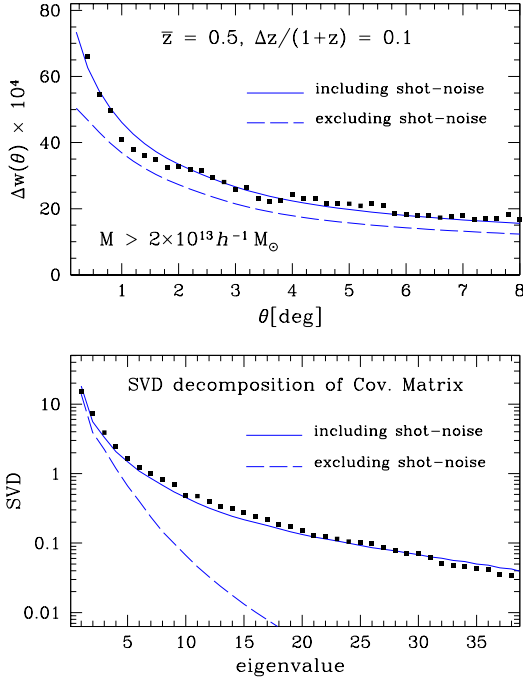


Figure 15. The effect of shot-noise at $z = 0.5$. Diagonal error (top panel) and Singular Value Decomposition of the Covariance Matrix (bottom panel) for the bin $z = 0.5$ and $\Delta z/(1+z) = 0.1$ for halos with $M > 2 \times 10^{13} h^{-1} M_{\odot}$. Conclusions shared with Fig. 14. We used 175 mocks for this test.

tom to rows of the reduced covariance matrix. Both set of measurements agree with each other. The ones with smaller $\Delta\theta$ seem slightly above in diagonal error and below in reduced covariance. But, as expected, they also show more noisy. In all, our model (shown in solid lines) describes both equally well.

7 CONCLUSIONS

The field of large scale cosmological structure will undergo an unprecedented era in the immediate future with several large observational campaigns proposed or under implementation. Many of these surveys, such as DES, PanStarrs and LSST, will use photometric techniques to estimate the radial position of galaxies instead of measuring their full spectra, which is more time-demanding. This gain allows to survey wider areas and fainter objects, but at the exchange of increasing the uncertainties in the true redshifts and degrading the radial clustering amplitude. The proposal is then to split the data into redshift bins and exploit the information available from angular correlation functions, provided with an accurate determination of the measurement errors. Yet, this goal can only be accomplished if we develop accurate models for the signal and its errors that take into account all relevant effects and are robustly tested in realistic scenarios. In this paper we addressed this issue in a comprehensive way.

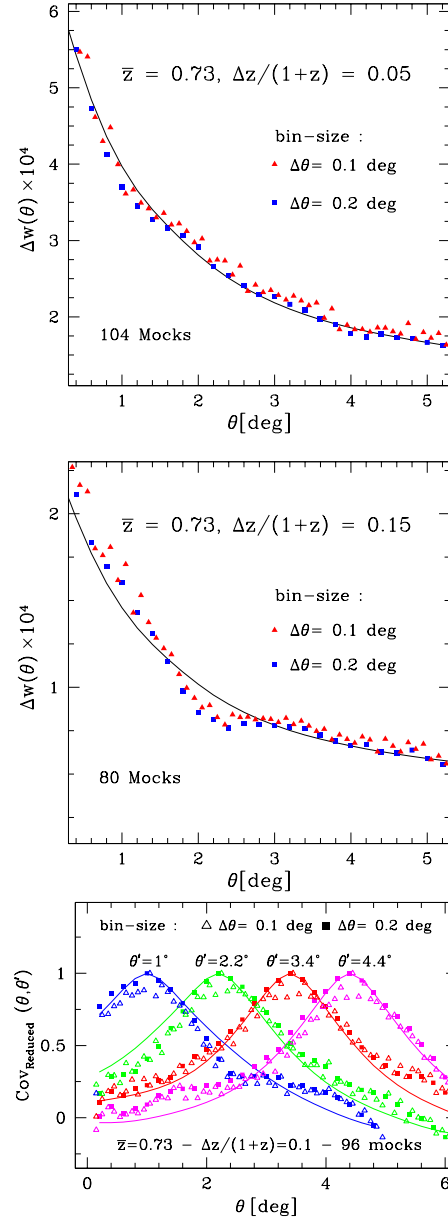


Figure 16. Independence on angular bin-size. The figure shows how the diagonal error (top two panels) and reduced covariance (bottom panel) vary when one halves the angular bin-size. Recovered correlations becomes noisier but no appreciable systematic difference with the model is found.

We first developed an extensive set of mock catalogues (in the form of redshift bins) reproducing the angular coverage and radial distribution of a photometric survey like DES. We did it in increasing steps of realism, first in real space, then including redshift distortions or photometric errors and finally altogether. For this we used a large N-body simulation (of $\sim 450 h^{-3} \text{Gpc}^3$ simulated volume) provided by the MICE collaboration (<http://www.ice.cat/mice>). These mocks can be regarded as independent realizations as their volume overlap is minimal and therefore provide a

unique statistical framework for model testing (see Table 1). We claim they are also equivalent to a light-cone analysis as we are doing narrow redshift bins, which involve negligible evolution.

We next put forward a model for the angular correlation function $w(\theta)$ accounting for all the relevant effects, namely bin projection, nonlinear gravitational evolution, linear bias, redshift space distortions and photo-z errors.

An exhaustive comparison of our model for $w(\theta)$ against the mock measurements showed a remarkably good agreement for a wide range of θ and scenario (real space, photo-z, RSD and photo-z + RSD), validating the treatment of the different effects and opening the door to the use of this probe for real data analysis. Nonlinear gravitational evolution produces minor distortions in the correlation pattern after the bin projection. In turn, analysis of halo angular clustering showed a very good consistency with a linear bias assumption. The interplay of photo-z and redshift distortions is the most important consideration regarding the shape of $w(\theta)$.

Redshift space distortions introduces a large and scale dependent enhancement of $w(\theta)$, that can reach a factor of a few at BAO scales (see Fig. 5). For our widest bin (where the effect should be least important) it still rises the amplitude of $w(\theta)$ by $\sim 50\%$ at θ_{BAO} (with respect to real space). Conversely, photo-z effects lower the clustering amplitude by extending the effective bin projection. For example, for the widest bin mentioned before (with $\Delta z \sim 4\sigma_z$) we find that the two effects counter-act each other at θ_{BAO} , but leave a scale dependent signal towards smaller angles. For narrower bins photo-z dominates, but redshift distortions is certainly not negligible. These trends were concluded from both, our photo-z + RSD mocks, and the analytical model.

In turn, we showed that the Limber approximation should not be used in precision analysis of large scale clustering as it leads to the incorrect shape of $w(\theta)$ in the full range of interesting scales, and severely misestimates the amplitude of the C_ℓ spectra for $\ell \lesssim 40 - 50$. This is convincingly shown in Figs. B1, B2 and B3. Another interesting issue considered was the impact of uncertainties in the true redshift distribution of objects. This showed an important aspect since it can lead to several percent changes in both the shape of $w(\theta)$ and the BAO peak position given the accuracy of present photo-z estimators.

We would like to highlight that, in the process of describing $w(\theta)$, we have also investigated a model for the 3-d matter correlation function that is able to reproduce the clustering signal in a broad range of scales and redshifts with only 2 parameters. This, discussed in detail in Appendix A, can be of grand interest for future spectroscopic surveys such as BOSS, Hetdex and WiggleZ.

We have made an equally exhaustive effort in modeling and testing the full error matrix characterizing the measurements of $w(\theta)$. The covariance matrix is often estimated from the data itself, using internal or re-sampling methods such as Jack-knife or bootstrapping. However, their limitation is still a matter of some debate (Norberg et al. 2009). Having a full theoretical model is thus very suitable for present and future analysis.

We took into account partial sky coverage by assuming

that $\text{Cov}(\theta, \theta')$ scales as f_{sky}^{-1} . The full sky situation is then easily treated by translating errors from harmonic space, where the covariance matrix is diagonal and proportional to C_ℓ . Through the angular power spectra we included the same effects considered for $w(\theta)$ into $\text{Cov}(\theta, \theta')$ (photo-z, redshift distortions, bias) for a typical survey with $f_{sky} = 1/8$.

Our modeling of errors recovers the correct variance in $w(\theta)$ as measured in the mocks for a wide range of bin configurations, from low to high redshift ($z \sim 0.3 - 1.1$) and from thin to thick bins ($100 h^{-1} \text{Mpc} - 550 h^{-1} \text{Mpc}$). And this conclusion extend to the more realistic cases where we included photo-z effects and redshift space distortions. In addition we used different halo samples to study cases where the shot-noise was comparable or larger than the sample variance component of the error. This regime was also nicely described analytically by adding a standard Poisson shot-noise contribution to the variance of the C_ℓ spectra.

Moreover, and thanks to the large number of mocks constructed, we measured the full covariance matrix with high precision in different configurations. We find that at least 150 – 200 mocks are necessary for a well defined reduced covariance, but this is discussed more properly in Cabré et al. 2010. Remarkably in all cases tested, the modeling recovers very accurately the true error matrix.

In a parallel line of research we have tested the recovery of cosmological parameters using our model for $w(\theta)$ and the theoretical expression of the covariance matrix. And compared this with the same analysis but using the *true covariance* as measured in the mock ensembles. Indeed, the best-fit values and errors contours coincide for both approaches (Cabré et al. 2010) giving very encouraging prospects for the use of our analytical expressions in real data analysis or in realistic forecasts of upcoming photometric surveys.

ACKNOWLEDGMENTS

We would like to thank the Large Scale Structure Working group of the Dark Energy Survey for motivating the core of this work. We are particularly thankful to Ashley Ross and Will Percival for stimulating discussions regarding redshift distortions, Pablo Fosalba for sharing his experience in angular statistics and Jorge Carretero for technical support with the simulation. Funding for this project was partially provided by the Spanish Ministerio de Ciencia e Innovación (MICINN), projects 200850I176, AYA2009-13936-C06 Consolider-Ingenio CSD2007-00060, research project 2005SGR00728 from Generalitat de Catalunya and the Juan de la Cierva MEC program. The mock catalogues essential to this paper were possible thanks to an N-body simulation provided by the MICE collaboration.

The ensemble of mock redshift bins taking into account photo-z effects and redshift distortions, as described in Table 1, will be publicly available at <http://www.ice.cat/mice>.

REFERENCES

- Abdalla, F. B., Banerji, M., Lahav, O., Rashkov, V., 2008, eprint arXiv:astro-ph/0812.3831
- Banerji, M., Abdalla, F. B., Lahav, O., Lin, H., MNRAS, **386**, 1219 (2008)
- Barriga, J., Gaztañaga, E., MNRAS, **333**, 443 (2002)
- Bernstein, G., ApJ, **424**, 569 (1994)
- Bernstein, G., Huterer, D., MNRAS, **401**, 1399 (2010)
- Bharadwaj, S., ApJ, **472**, 1 (1996)
- Blake, C., Collister A., Bridle S., Lahav, O., MNRAS, **374**, 1527 (2007)
- Budavári, T., et al., ApJ, **595**, 59 (2003)
- Cabré, A., Fosalba, P., Gaztañaga, E., Manera, M., MNRAS, **381**, 1347 (2007)
- Cabré, A., Crocce, M., Gaztanāga, E., *in prep.* (2010)
- Cabré, A., Gaztanāga, E., MNRAS, **393**, 1183, (2009)
- Cai, Y-C, Angulo, R. E., Baugh, C. M.; Cole, S., Frenk, C. S., Jenkins, A., MNRAS, **395**, 1185 (2009)
- Cole, S., et al., MNRAS, **362**, 505 (2005)
- Colless M., et al., e-print arXiv:astro-ph/0306581 (2003)
- Crocce, M., Fosalba, P., Castander, F. J., Gaztañaga, E., MNRAS, **403**, 1353 (2010)
- Crocce, M. and Scoccimarro, R., PRD, **73**, 063519 (2006a)
- Crocce, M. and Scoccimarro, R., PRD, **73**, 063520 (2006b)
- Crocce, M. and Scoccimarro, R., PRD, **77**, 023533 (2008)
- Desjacques, V., Sheth, R. K., PRD, **81**, 023526 (2010)
- Desjacques, V., Crocce, M., Scoccimarro, R., Sheth, R. K., PRD, **82**, 103529 (2010)
- Dodelson S., *Modern Cosmology*, p. 342 Eq. 11.27, Academic Press Inc., U.S. (2003)
- Eisenstein, D. J., Zaldarriaga, M., MNRAS, ApJ, **546**, 2 (2001)
- Eisenstein, D. J., et al., M., ApJ, **633**, 560 (2005)
- Eisenstein, D. J., Seo, H-J., White, M., ApJ, **664**, 660 (2007)
- Eriksen, H. K., Lilje, P. B., Banday, A. J., Gorski, K. M., ApJS, **151**, 1 (2004)
- Evrard A. E., et al., ApJ, **573**, 7, (2002)
- Fisher, K. B., Scharf, C. A., Lahav, O., MNRAS, **266**, 219 (1994)
- Fosalba, P., Gaztañaga, E., Castander, F. J., Manera, M., MNRAS, **391**, 435 (2008)
- Fry, J. N., ApJ, **461**, L65+, (1996)
- Gaztañaga, E., Cabré, A., Hui, L., MNRAS, **399**, 1663 (2009)
- Górski, K. M., Hivon, E., Wandelt, B. D., in Proc. MPA-ESO Conf., Evolution of Large-Scale Structure: From Re-combination to Garching, p.37, (1999). Ed. A.J.Banday, R.K.Seth, and L.A.N. da Costa (Enschede: PrintPartners Ipskamp)
- Hearin, A. P., Zentner, A. R., Ma, Z., Huterer, D., ApJ **720**, 1351 (2010)
- Hamilton, A. J. S., ApJ, **385**, L5 (1992)
- Kaiser, N., MNRAS, **227**, 1 (1987)
- Kaiser, N., ApJ, **388**, 272 (1992)
- Kaiser, N., ApJ, **498**, 26 (1998)
- Komatsu, E., et al., ApJS, **192**, 18 (2011)
- Limber, D. N., ApJ, **117**, 134 (1953)
- LoVerde, M., Afshordi, N., PRD, **78** 123506 (2008)
- Ma, Z., Hu, W., Huterer D., ApJ, **636**, 21 (2006)
- Manera, M., Gazatanāga, E., e-print arXiv:astro-ph/0912.0446 (2009)
- Matarrese, S., Pietroni, M., Modern Phys. Letters A., **23**, 25 (2008)
- Matsubara, T., ApJ, **615**, 573 (2004)
- Matsubara, T., PRD, **77**, 06330 (2008)
- Meneux, B. et al., A&A, **505**, 463 (2009)
- McDonald, P., Trac, H., Contaldi, C., MNRAS, **336**, 547 (2006)
- Nock, K., Percival, W. J., Ross, A. J., MNRAS, **407**, 520 (2010)
- Norberg, P., Baugh, C. M., Gaztañaga, E., Croton, D. J., MNRAS, **396**, 19 (2009)
- Padmanabhan, N. et al., MNRAS, **359**, 237 (2005)
- Padmanabhan, N. et al., MNRAS, **378**, 852 (2007)
- Peebles, P. J. E., ApJ, **185**, 413 (1973)
- Percival, W. J., et al., MNRAS, **401**, 2148 (2010)
- Perlmutter, S., et al., ApJ, **517**, 565 (1999)
- Reid, B., et al., MNRAS, **404**, 60 (2010)
- Riess, A.G., et al., ApJ, **116**, 1009 (1998)
- Ross, N. P. et al, MNRAS, **381**, 573 (2007)
- Ross, A. J., Percival, Crocce, , Cabré, A., Gaztañaga, E., *in prep.*
- Sánchez, A. G., Baugh, C. M., Angulo, R., MNRAS, **390**, 1470 (2008)
- Sánchez, A. G., Crocce, M., Cabré, A., Baugh, C. M., Gaztañaga, E., MNRAS, **400**, 1643 (2009)
- Sánchez, E., Carnero, A., García-Bellido, J., Gaztañaga, E., de Simoni, F., Crocce, M., Cabré, A., Fosalba, P., Alonso, D., MNRAS, **411**, 277 (2011)
- Sawangwit, U., Shanks, T., Abdalla, F. B., Cannon, R. D., Croom, S. M., Edge, A. C., Ross, Nicholas P., Wake, D. A., MRAS *submitted*, e-print arXiv:astro-ph/0912.0511 (2009)
- Seo, H-J., Eisenstein, D. J., ApJ, **633**, 575 (2005)
- Simpson, F., Peacock, J. A., Simon, P., PRD, **79**, 063508 (2009)
- Smith, R., Scoccimarro, R., Sheth, R. K., PRD, **77**, 043525 (2008)
- Springel, V., MNRAS, **364**, 1105 (2005)
- Szapudi, I., Prunet, S., Colombi, S., ApJ, **561**, L11 (2001)
- Taruya, A., Nishimichi, T., Saito, S., Hiramatsu, T., PRD, **80**, 123503 (2009)
- Thomas, S. A.; Abdalla, F. B.; Lahav, O., MNRAS *accepted*, eprint arXiv:astro-ph/1011.2448
- York D.G., et al., ApJ, **120**, 1579 (2000)

APPENDIX A: SPATIAL CLUSTERING

In Sec. 2.2 we presented a parametric model for the spatial correlation function and argued that a single set of best-fit parameters could be used to describe the clustering from low to high redshift. In this appendix we show how this model performs against measurements of 3-d clustering in N-body simulations, in particular *as a function of redshift*.

A0.1 Nonlinear Gravitational Clustering

The top panel of Fig. A1 shows the spatial correlation function measured in MICE7680 at $z = 0.3$ compared with the parametric model given in Eq. (10) for best-fit parameters $s_{bao} = 5.54 h^{-1} \text{Mpc}$ and $A_{mc} = 1.55$. To simplify the measurement we only used a cubic sub-volume of the full comoving output, of length $L_{\text{box}} = 2560 h^{-1} \text{Mpc}$. Error bars were obtained from the scatter among 125 Jack-knife volumes of the full box. We see that the model performs very well down to scales $\sim 20 h^{-1} \text{Mpc}$ at this redshift. Notice how the convolution of linear theory with a Gaussian smoothing (dot dashed line) leads to a slight increase in amplitude above the measurements for $r \lesssim 60 h^{-1} \text{Mpc}$. Measurements follow linear theory at these scales. The effect of the mode-coupling term in Eqs. (8,10) is mainly to correct for this mismatch.

From theoretical grounds we expect the smoothing length to be determined by the amplitude of large-scale velocity flows and therefore given by (Bharadwaj 1996; Crocce

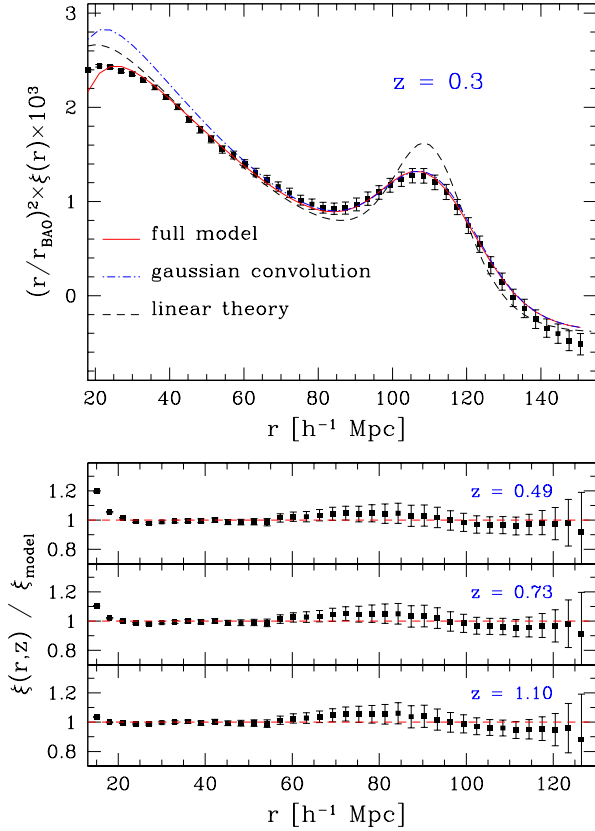


Figure A1. *Spatial Correlation Function:* measured in the $z = 0.3$ comoving output of a large volume N-body run (MICE7680) compared with the parametric model given in Eq. (8) with best-fit parameters $s_{bao} = 5.54 h^{-1} \text{ Mpc}$ and $A_{mc} = 1.55$ (Top panel). The length scale used in the y-axis is $r_{BAO} = 110 h^{-1} \text{ Mpc}$. Bottom panels display the ratio of the measured correlation function (at the given redshift) to our model correlation, obtained after scaling with redshift the $z = 0.3$ best-fit values.

and Scoccimarro 2006b; Eisenstein et al. 2007; Matsubara 2008),

$$s_{bao} \sim [(1/3) \int d^3 q P_{\text{Lin}}(q)/q^2]^{1/2} = 5.42 \text{ Mpc } h^{-1} \quad (\text{A1})$$

which is within 3% agreement with the recovered best-fit value. In turn, the lowest order estimation for A_{mc} using perturbation theory yields $34/21 \sim 1.62$ independently of cosmology and redshift (Crocce and Scoccimarro 2008), which is also very close to our best-fit value 1.55.

Hence, it is possible to use these theoretical estimates as a starting point in the modeling instead of using fitting parameters. Notice however that, if one extrapolates this model to describe the clustering of tracers, the actual values for s_{bao} and A_{mc} might depend on the particular tracer under study (e.g. on halo mass) (Sánchez et al. 2008). In addition, the rather large error bars obtained from present day data do not put severe constraints on the values of s_{bao} and A_{mc} (Sánchez et al. 2009; Percival et al. 2010).

As discussed in Sec. 2.2 one interesting aspect of a theoretical model when it comes to analyze data split into con-

tinuous redshift bins is the possibility to understand the redshift evolution of the nuisance parameters involved, which in turn allows one to fit the least number of parameters (i.e. just at one fiducial redshift). With this approach in mind we now show that our model can indeed describe the 3-d clustering from low to high redshift using a single set of best-fit parameters. And this property will remain after the projection into angular correlations in Eq. (5).

The bottom panel of Fig. A1 shows our model in Eq. (10) against measurements of ξ in the comoving outputs of MICE7680 at $z = 0.5, 0.73$ and 1.1 . The values for s_{bao} and A_{mc} were taken from a best-fit analysis to $\xi(r)$ at $z = 0.3$. In all cases the agreement is very good, similar to that at $z = 0.3$.

Notice that conclusion in this appendix relate to 3-d clustering in general, regardless of photo- z , hence are also relevant for spectroscopic surveys such as BOSS¹³, Hetdex¹⁴ and WiggleZ¹⁵.

APPENDIX B: THE LIMBER APPROXIMATION

B1 C_ℓ power spectrum : exact evaluation and Limber formula

In this appendix we discuss the way we implement the numerical integrations that lead to the exact C_ℓ spectra in Eqs. (19,20), and how this exact result compares with the widely used Limber approximation (Limber 1953).

Let us first recall the derivation of the exact expression of the angular power spectrum in terms of the spatial one. This is done by expanding the density field in Eq. (1) in Fourier Series and subsequently expanding the plane wave into spherical harmonics¹⁶. After some straightforward manipulation this leads to,

$$a_{\ell m} = 4\pi i^\ell \int dz \phi(z) \int \frac{d^3 k}{(2\pi)^3} \delta(\mathbf{k}, z) j_\ell(kr(z)) Y_{\ell m}^*(\hat{\mathbf{k}}), \quad (\text{B1})$$

where j_ℓ are the spherical Bessel functions of order ℓ . Inserting Eq. (B1) into Eq. (13) and using the orthogonality relation of the spherical harmonics gives Eqs. (19,20),

$$C_{\ell, \text{Exact}} = \frac{1}{2\pi^2} \int 4\pi k^2 dk P(k) \Psi_\ell^2(k)$$

$$\Psi_\ell(k) = \int dz \phi(z) D(z) j_\ell(kr(z))$$

These integral expressions are numerically expensive to compute due to the oscillatory behavior of the spherical Bessel functions $j_\ell(x)$ for $x \gg 1$. It is then desirable to seek for ways to improve their convergence. The most popular short-cut to evaluate Eqs. (19,20) is the so-called Limber approximation (Limber 1953; Kaiser 1992; Kaiser 1998)

¹³ <http://www.sdss3.org/>

¹⁴ <http://hetdex.org/>

¹⁵ <http://wigglez.swin.edu.au/>

¹⁶ $e^{i\mathbf{k}r\hat{\mathbf{k}}\cdot\hat{\mathbf{n}}} = 4\pi \sum_{\ell \geq 0} \sum_{m=-\ell}^{\ell} i^\ell j_\ell(kr) Y_{\ell m}(\hat{\mathbf{k}}) Y_{\ell m}^*(\hat{\mathbf{n}})$

that follows from the orthogonality relation of the spherical Bessel functions (e.g. see Loverde and Afshordi 2008),

$$\int dk k^2 j_l(kr_1) j_l(kr_2) P(k) \quad (\text{B2})$$

$$\approx \frac{\pi}{2} \frac{\delta^D(r_1 - r_2)}{r_1^2} P(k = \frac{l + 1/2}{r}),$$

that leads to the well-known expression,

$$C_{\ell, \text{Limber}} = \int dz \phi^2(z) D^2(z) P((\ell + 1/2)/r(z)) \frac{AM(z)}{r(z)^2}. \quad (\text{B3})$$

Strictly speaking this is valid for $\ell \gg 1$ (that is, small angles), but in practice it coincides with the exact expression already by $\ell \sim 50 - 100$ as discussed in Fig. B1 (see also Blake et al. 2007; Loverde and Afshordi 2008). Therefore we proceed as follows. First, let us concentrate on linear theory fluctuations. Then, inspired by Eq. (8) (and Crocce and Scoccimarro 2006b; Eisenstein et al. 2007; Matsubara 2008) we decompose the *linear* power spectrum as

$$P(k) = P_{\text{Lin}}(k)G(k) + P_{\text{Lin}}(k)(1 - G(k)), \quad (\text{B4})$$

with $G = \exp(-k^2 s_{ba0}^2)$ and s_{ba0} taken from Eq. (A1). The first term dominates at large scales and accounts for the degradation of BAO bump, leading also to the correct shape of the 3-d correlation function in a broad range of scales (Fig A1). Since this is our regime of interest we evaluate this piece using the exact integration, that can now be integrated up to an upper bound such that $k_{\text{max}} s_{ba0} \sim 4 - 5$ where $P_{\text{Lin}} \exp(-k^2 s_{ba0}^2)$ is already suppressed by several orders of magnitude. The second term in Eq. (B4) is non-negligible only at high- ℓ therefore it can be computed using the Limber formula, Eq. (B3). In all, we evaluate the exact C_ℓ as ¹⁷

$$C_\ell = C_{\ell, \text{Exact}}(P_{\text{Lin}} \times G) + C_{\ell, \text{Limber}}(P_{\text{Lin}} \times (1 - G)) \quad (\text{B5})$$

In the top panel of Fig. B1 we show the average C_ℓ power spectrum measured in 324 *real space* mocks centered at $\bar{z} = 0.5$ with $\Delta z/(1+z) = 0.05$ (using SpICE, see Szapudi et al. 2001), and compare it with the exact integration (solid blue line) and the Limber evaluation (solid red line) of the first term of Eq. (B4). Clearly, the Limber approximation fails by a large factor at low- ℓ , which is in broad agreement with the literature (Blake et al. 2007; Loverde and Afshordi 2008). However, by $\ell \sim 60$ it fully coincides with the exact computation. The contribution of the second term in Eq. (B4) is only relevant for $\ell > 100$ (dashed black line) and therefore it is safely computed using the Limber approximation. We have checked that these conclusions remain true for different \bar{z} and Δz . Bottom panel of Fig. B1 shows the full C_ℓ -Limber (red plus dashed lines in top panel) and the measured spectra in ratio with our model for the exact C_ℓ spectra, given by Eq. (B5) (i.e. blue plus dashed in top panel).

Notice that we have only attempted to evaluate the *linear* spectrum. Nonlinear effects can be taken into account by replacing P_{Lin} in Eq. (B4) by fits to nonlinear

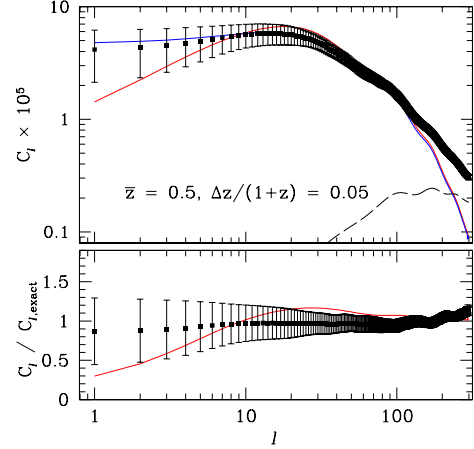


Figure B1. Top Panel: Angular Power Spectrum measured in 324 *Real Space* mock catalogues of mean redshift $\bar{z} = 0.5$ and width $\Delta z/(1+z) = 0.05$, compared with our theoretical estimate, which we brake into to additive contributions (Eq. B5), low- ℓ from the exact integration in Eq. (19) (solid blue line) and large- ℓ from the Limber approximation in Eq. (B3) (dashed black line). Solid red line shows the low- ℓ term computed with the Limber approximation, which leads to a severe under-estimation of the large angle power ($l \leq 30$). This could critically impact the computation of $w(\theta)$ and its covariance at large BAO scales. Bottom Panel: Ratio of the full C_ℓ -Limber (red line) and the measurements to our estimation of the exact (linear theory) C_ℓ spectra. Displayed error bars correspond to the ensemble r.m.s variance.

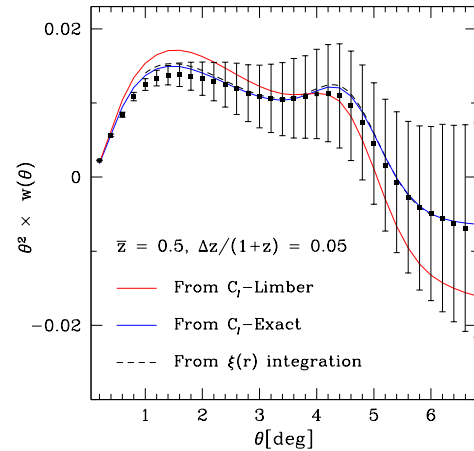


Figure B2. *Angular Correlation Function* measured in the 324 mock bins compared with the theoretical predictions obtained from Eq. (5) (dashed line), or from C_ℓ -space through the Legendre polynomials and Eq. (14). Using the Limber approximation to compute the C_ℓ leads an incorrect shape for $w(\theta)$ (solid red line). In turn, the exact C_ℓ integration agrees as expected with Eq. (5) (solid blue line). Displayed error bars correspond to the ensemble r.m.s variance.

¹⁷ The difference between our approach and a straightforward use of the exact integration for all the ℓ range is under 1%.

power spectrum, such as **halofit**, or exact analytical expressions (Crocce and Scoccimarro 2006a; Matarrese & Pietroni 2008; Matsubara 2008; Taruya et al. 2009). However we have found that for our purposes this gave no additional contributions to the error estimations. In fact, the second term in Eq. (B5) had a negligible impact in the estimate of $\Delta w(\theta)$ for all cases we had considered. It only gave a contribution when evaluating the covariance matrix in cases where the shot-noise of the sample under consideration is fully negligible (see Sec. 6.3). We finish by noting that linear redshift space distortions fully cancel for large ℓ (Padmanabhan et al. 2007), therefore they only need to be accounted for in the first term of Eq. (B5) (following Eq. 21).

B2 Correlation Function : results in Real and Redshift Space

The inaccuracy of the Limber approximation also affects the calculations in configuration space. For instance, the way in which the disagreement in Fig B1 translates into Real Configuration Space is depicted in Fig. B2. Solid red and solid blue lines were obtained using Eq. (14) and C_ℓ from the Limber or the Exact evaluation respectively (those shown in top panel of Fig. B1). Dashed line follows from projecting the corresponding 3-d correlation function, as in Eq. (5). Here, the failure of the Limber approximation to describe the BAO bump is more evident. The exact C_ℓ integration yields the same result as the one from Eq. (5), as expected.

These limitations are even more severe when redshift distortions are taken into account. Without loss of generality we will use a top-hat selection in the following equations to illustrate the problem:

$$w(\theta) = \frac{1}{\Delta_\chi^2} \int_{\chi_{min}}^{\chi_{max}} d\chi_1 \int_{\chi_{min}}^{\chi_{max}} d\chi_2 \xi(r_1, r_2) \quad (B6)$$

where $\Delta_\chi \equiv \chi_{max} - \chi_{min}$. The correlation $\xi(r_1, r_2)$ is only a function of the relative separation between r_1 and r_2 . Because of redshift distortions, this is in fact a function of π and σ , the light-of-sight and transverse separation. For small angles and distance observer, i.e. the Limber approximation, we can take $\pi = \chi_2 - \chi_1$ and $\sigma^2 = \chi_1 \chi_2 \theta^2$ ¹⁸. We can then change variables in the above integrals from χ_1 and χ_2 to π and σ

$$w(\theta) = \frac{2}{\theta \Delta_\chi^2} \int_{\sigma=\chi_{min}\theta}^{\sigma=\chi_{max}\theta} d\sigma \int_{\pi=0}^{\pi=\Delta_\chi} d\pi \xi(\pi, \sigma) \quad (B7)$$

This result is valid both in real and redshift space. In real space, $\xi(\pi, \sigma)$ is replaced by the isotropic correlation $\xi(r)$ with $r^2 = \pi^2 + \sigma^2$. In redshift space we use the linear theory prediction (Kaiser 1987; Hamilton 1992):

$$\xi(\sigma, \pi) = \xi_0(s)P_0(\mu) + \xi_2(s)P_2(\mu) + \xi_4(s)P_4(\mu) \quad (B8)$$

where π and σ represent the separation along and transverse

to the line-of-sight (l.o.s) and ξ_ℓ are the multi-poles of the correlation function in terms of Legendre polynomials P_ℓ ,

$$\xi_\ell(s) = \frac{2\ell+1}{2} \int_{-1}^{+1} \xi(\pi, \sigma) P_\ell(\mu) d\mu, \quad (B9)$$

with $s = \sqrt{\sigma^2 + \pi^2}$ and μ is the cosine angle with the l.o.s. For the Kaiser model one has (Hamilton 1992),

$$\xi_0(s) = b^2 \left(1 + \frac{2\beta}{3} + \frac{\beta^2}{5} \right) \xi(s) \quad (B10)$$

$$\xi_2(s) = b^2 \left(\frac{4\beta}{3} + \frac{4\beta^2}{7} \right) [\xi(s) - \xi(\bar{s})] \quad (B11)$$

$$\xi_4(s) = b^2 \frac{8\beta^2}{35} \left[\xi(s) + \frac{5}{2} \xi(\bar{s}) - \frac{7}{2} \xi(\bar{\bar{s}}) \right] \quad (B12)$$

where b is the bias of the sample (assumed linear and local), $\beta = f/b$, $f = \partial \ln D / \partial \ln a$ is the growth rate factor and

$$\xi(\bar{r}) = \frac{3}{r^3} \int_0^r \xi(r') r'^2 dr', \quad (B13)$$

$$\xi(\bar{\bar{r}}) = \frac{5}{r^5} \int_0^r \xi(r') r'^4 dr'. \quad (B14)$$

We will show next that Eq. (B7) turns out to be a bad approximation to model BAO scales. But it provides a good way to illustrate why redshift space distortions are so important for the BAO detection for small (to moderate) photo-z bin widths Δ_χ . For large values of Δ_χ the integral reproduces the real space correlation (because the total number of pairs are preserved by redshift space distortions), while for $\Delta_\chi < 500 h^{-1}$ Mpc the π integral is truncated by the radial boundary of the top-hat window. Line-of-sight pairs separated by $\pi > \Delta_\chi$ do not enter in the redshift bin and are therefore not integrated. Smaller pairs are also affected because many of them are missing at the boundaries. This missing pairs produce a distortion in the measured $w(\theta)$ as compared to real space correlation (see Fisher et al. 1994, Padmanabhan et al. 2007 and Nock et al. 2010).

Both real and redshift results are quite inaccurate under the Limber approximations. This is illustrated in Fig. B3, which compares the calculation of the above integral in real and redshift space in the Limber approximation (dashed lines) with the corresponding exact results (continuous line) by integrating Eq. (B6). Note how the results in real space are very similar to the corresponding calculation in Fig. B2, based on power spectrum calculation. The results in redshift space for the Limber approximations show even larger deviations than in real space. The BAO peak, which shows around $\theta \simeq 4^\circ$ is clearly distorted by the Limber approximation. We conclude that the Limber approximation is not good enough for precision BAO modeling and we use the exact integration throughout this paper.

APPENDIX C: ERRORS IN HARMONIC SPACE

In this appendix we comment briefly on the correlation between different modes in Harmonic Space induced by a partial sky coverage.

¹⁸ For a non-flat cosmology we need to replace χ by the comoving angular diameter $D(\chi)$ distance here: $\sigma^2 = D(\chi_1)D(\chi_2)\theta^2$

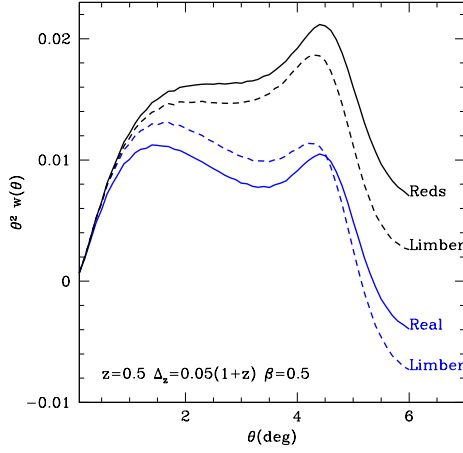


Figure B3. Angular correlation in the Limber approximation (dashed line) in Eq. (B7) in both real (bottom dashed line) and redshift space (top dashed line). Continuous lines show the corresponding exact calculations using Eq. (B6).

Equation (18) can be naively interpreted as if, in the presence of a partial sky coverage, the errors in C_ℓ increase by a factor $1/\sqrt{f_{\text{sky}}}$, that is

$$(\Delta C_\ell)^2 \approx \frac{1}{f_{\text{sky}}} \frac{2}{2\ell+1} C_\ell^2, \quad (\text{C1})$$

with the co-variance matrix remaining diagonal. In reality, the presence of boundaries *decreases* the diagonal error but it also introduces co-variance between different ℓ modes (e.g. Cabré et al. 2007 and references therein).

This is clearly depicted in Figure C1 where we show the error in Harmonic space from C_ℓ measurements using 392 mocks with $\bar{z} = 0.5$ and $\Delta z/(1+z) = 0.1$, and compared them with the expression above. Top panel corresponds to the measured diagonal error, which indeed is much smaller than that from the naive interpretation in Eq. (C1) given by the dashed line (even smaller than the full-sky limit shown in solid line). Bottom panel, corresponding to $\text{Cov}(\ell, \ell')$ for fixed values of ℓ' , shows the emergence of co-variance between different modes distributed in a range of ℓ values approximately given by $\pm 1/f_{\text{sky}}$. In all, the “total error” is larger than in full-sky.

This conclusion can be naively founded from the fact that for a given value of ℓ' the integral,

$$\int d\ell \text{Cov}(\ell', \ell) \approx \frac{2}{f_{\text{sky}}(2\ell'+1)} C_{\ell'}^2 \quad (\text{C2})$$

what leads to the simple interpretation that, when the survey is reduced from a full-sky limit by a fraction f_{sky} , the diagonal covariance rises from its value $2/(2\ell+1)$ by a factor $1/f_{\text{sky}}$ but then “leaks” towards other ℓ modes resulting in a non-diagonal error matrix. The final diagonal error is smaller than its “full-sky” value but is the off-diagonal elements of $\text{Cov}(\ell, \ell')$ what determine $\text{Cov}(\theta, \theta')$. Yet, we circumvent the problem of computing non-diagonal components of $\text{Cov}(\ell, \ell')$ by assuming the scaling of the covariance in Configuration space as $1/f_{\text{sky}}$.

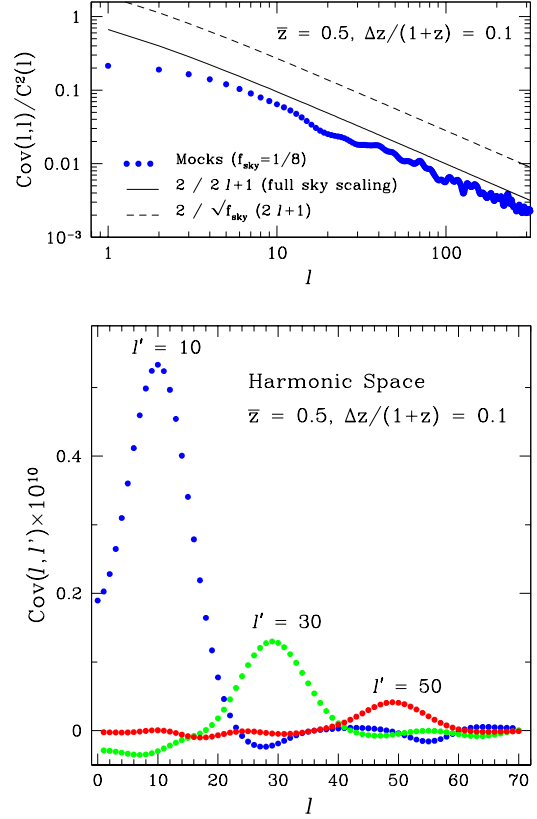


Figure C1. Correlations of C_ℓ spectra induced by partial sky coverage. The total error budget in a partial sky survey increases (roughly by a factor $1/f_{\text{sky}}$) compared to the full sky case. The covariance matrix is no longer diagonal (bottom panel) with the variance error smaller than its full sky value, by 30% in this particular case, as shown in the top panel (see text for details).

A standard way to overcome the complex covariance in Harmonic Space is to bin the measured C_ℓ spectra in such a way to make the covariance matrix block-diagonal (e.g. Cabré et al. 2007). A simple rule of thumb discussed in Cabré et al. 2007 is to choose $\Delta\ell f_{\text{sky}} \sim 2$, which is in very nice agreement with the width of the $\text{Cov}(\ell, \ell')$ distribution in Fig. C1. It remains to be studied whether this have an impact in methods like BAO where one is after short-wavelength features on top of the broad band C_ℓ shape.